US 20240158899A1

(19) **United States**

(12) **Patent Application Publication**

Beura et al.

(10) **Pub. No.: US 2024/0158899 A1**

(43) **Pub. Date: May 16, 2024**

(54) **SURFACE ATTRITION TREATMENT, COMPOSITIONS, AND METHODS OF USE THEREOF**

(71) Applicants: **ARIZONA BOARD OF REGENTS ON BEHALF OF ARIZONA STATE UNIVERSITY**, Scottsdale, AZ (US); **DEVCOM Army Research Laboratory**, Aberdeen, MD (US)

(72) Inventors: **Vikrant Beura**, Tempe, AZ (US); **Kiran Solanki**, Tempe, AZ (US); **Kris Darling**, Aberdeen, MD (US)

(21) Appl. No.: **18/388,317**

(22) Filed: **Nov. 9, 2023**

Related U.S. Application Data

(60) Provisional application No. 63/424,041, filed on Nov. 9, 2022.

Publication Classification

(51) **Int. Cl.**

C22F 1/057	(2006.01)
B24C 1/10	(2006.01)
C22C 21/00	(2006.01)
C22C 21/02	(2006.01)
C22C 21/14	(2006.01)
C22C 21/16	(2006.01)
C22C 30/02	(2006.01)
C22F 1/04	(2006.01)
C22F 1/043	(2006.01)
C22F 1/16	(2006.01)

(52) **U.S. Cl.**

CPC ***C22F 1/057*** (2013.01); ***B24C 1/10*** (2013.01); ***C22C 21/00*** (2013.01); ***C22C 21/02*** (2013.01); ***C22C 21/14*** (2013.01); ***C22C 21/16*** (2013.01); ***C22C 30/02*** (2013.01); ***C22F 1/04*** (2013.01); ***C22F 1/043*** (2013.01); ***C22F 1/16*** (2013.01)

(57) **ABSTRACT**

The present invention relates to surface attrition treatment, compositions, and methods of use thereof.

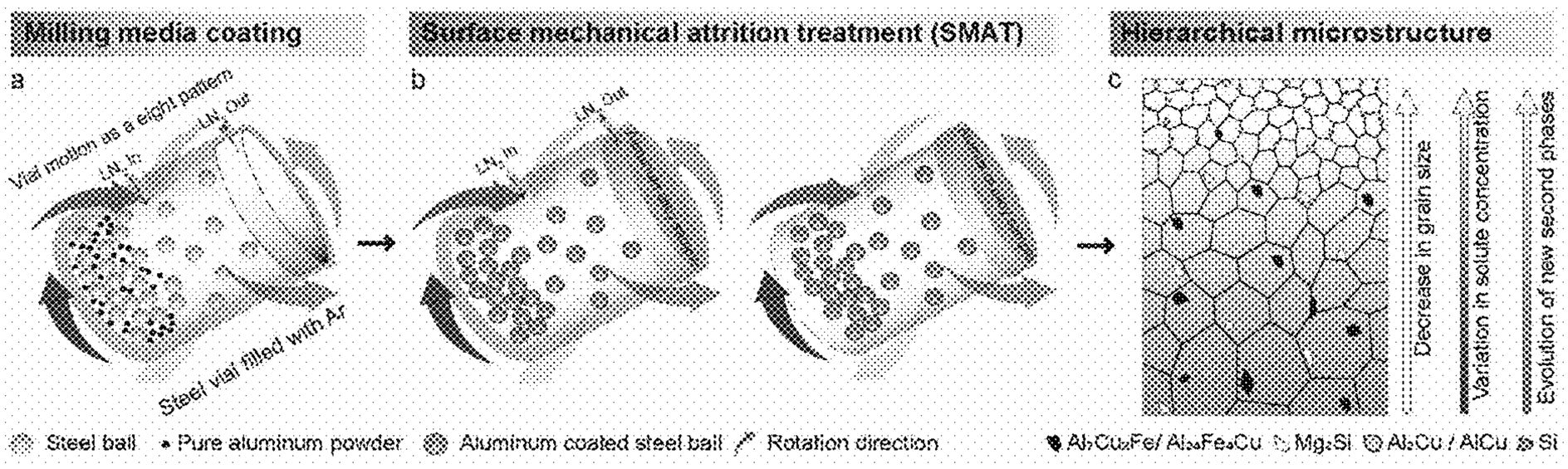

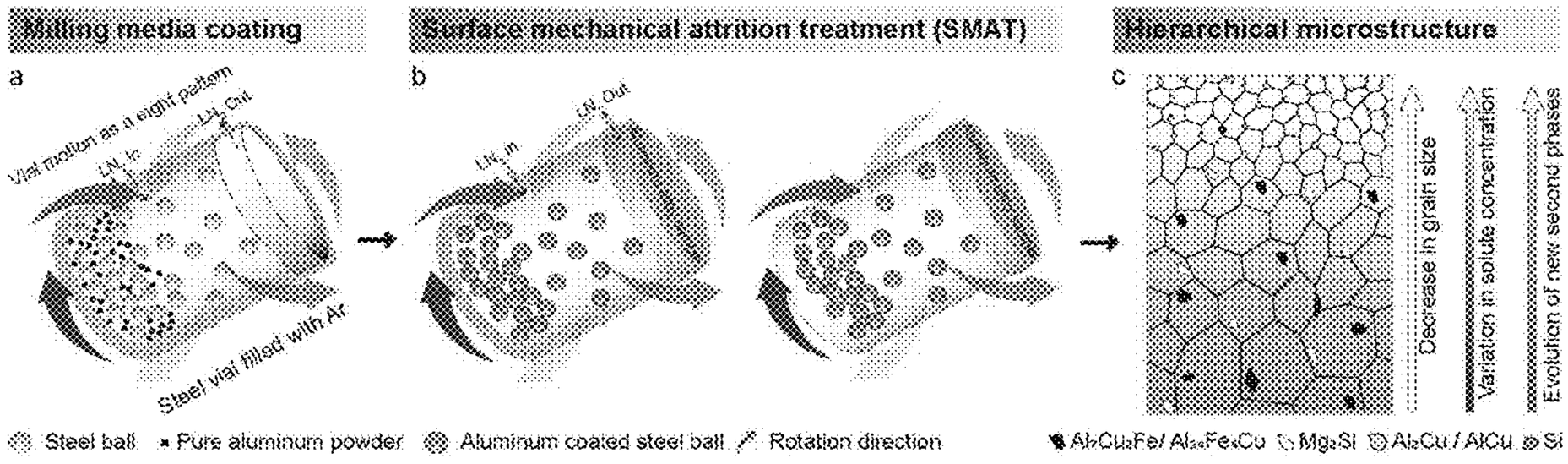
Milling media coating
Surface mechanical attrition treatment (SMAT)
Hierarchical microstructure
a
b
c
Vial motion as a eight pattern
LN2 In
LN2 Out
Steel vial filled with Ar
LN2 In
LN2 Out
Decrease in grain size
Variation in solute concentration
Evolution of new second phases
Steel ball
Pure aluminum powder
Aluminum coated steel ball
Rotation direction
Al7Cu2Fe/ Al13Fe4Cu
Mg2Si
Al2Cu / AlCu
Si

Figure 1

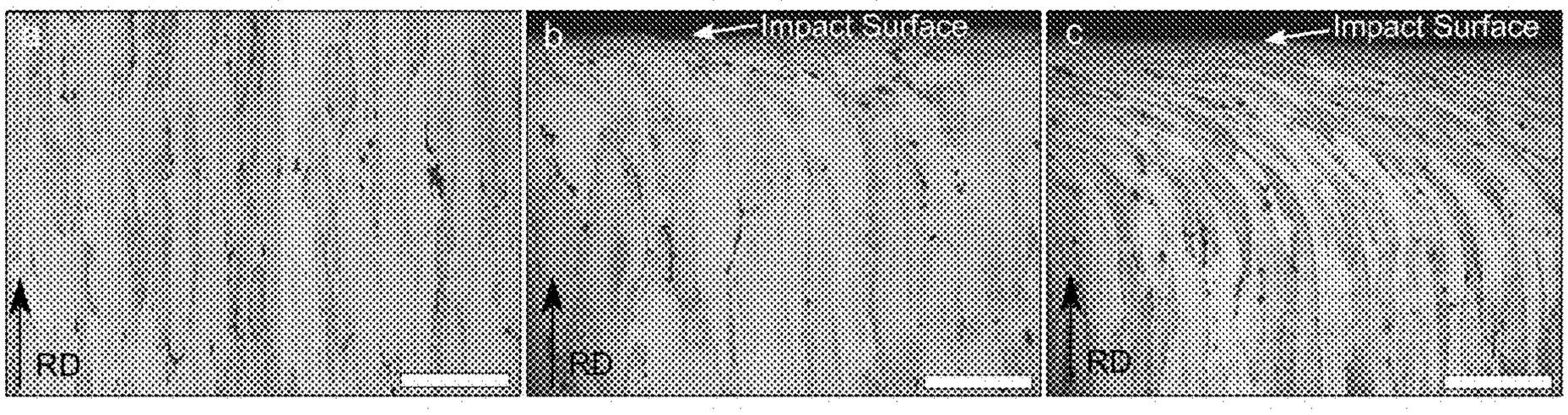

Figure 2

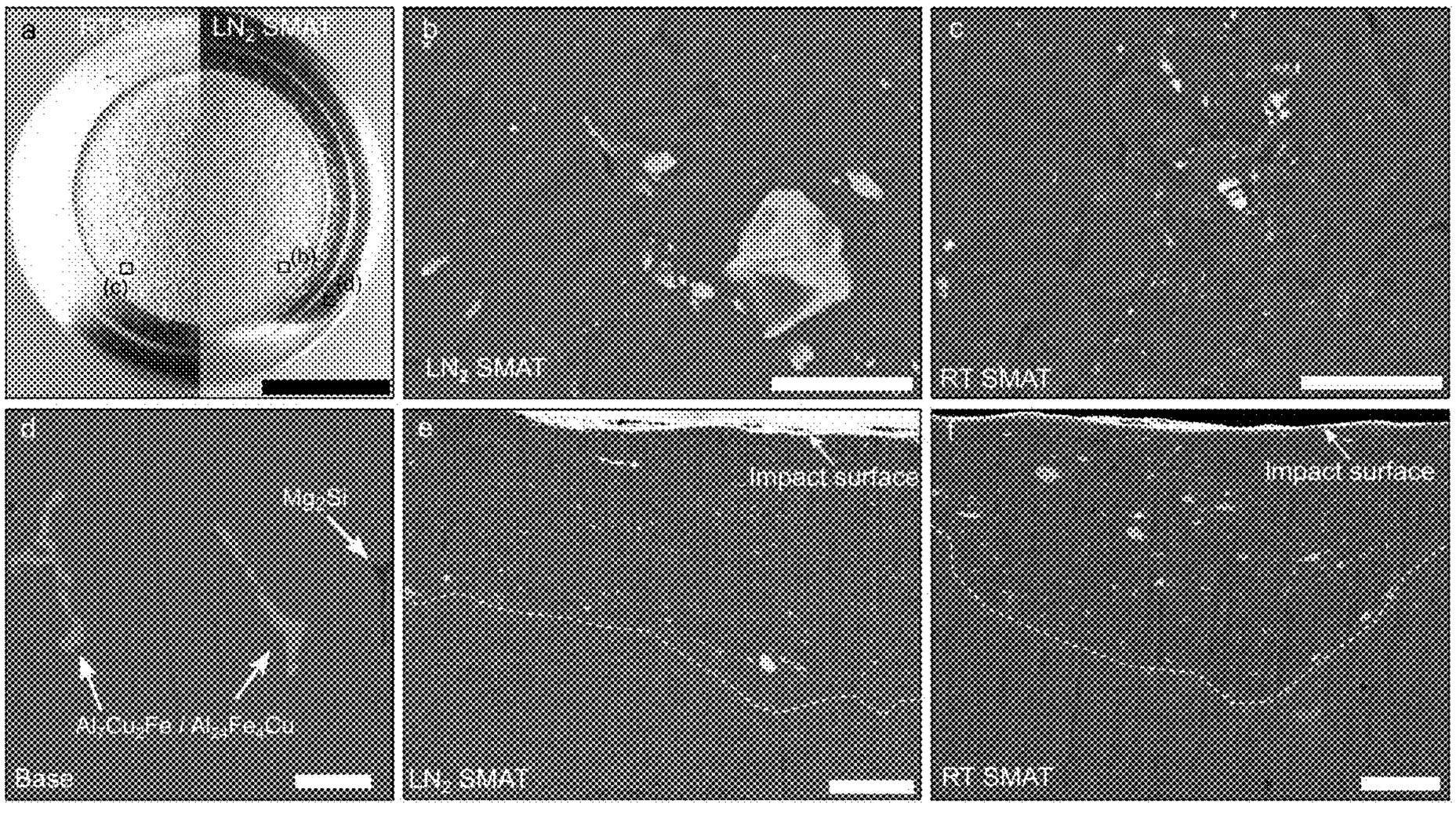
a
LN2 SMAT
(c)
(b)
(d)
b
LN2 SMAT
c
RT SMAT
d
Mg2Si
Al7Cu2Fe / Al2Fe3Si
Base
e
Impact surface
LN2 SMAT
f
Impact surface
RT SMAT

Figure 3

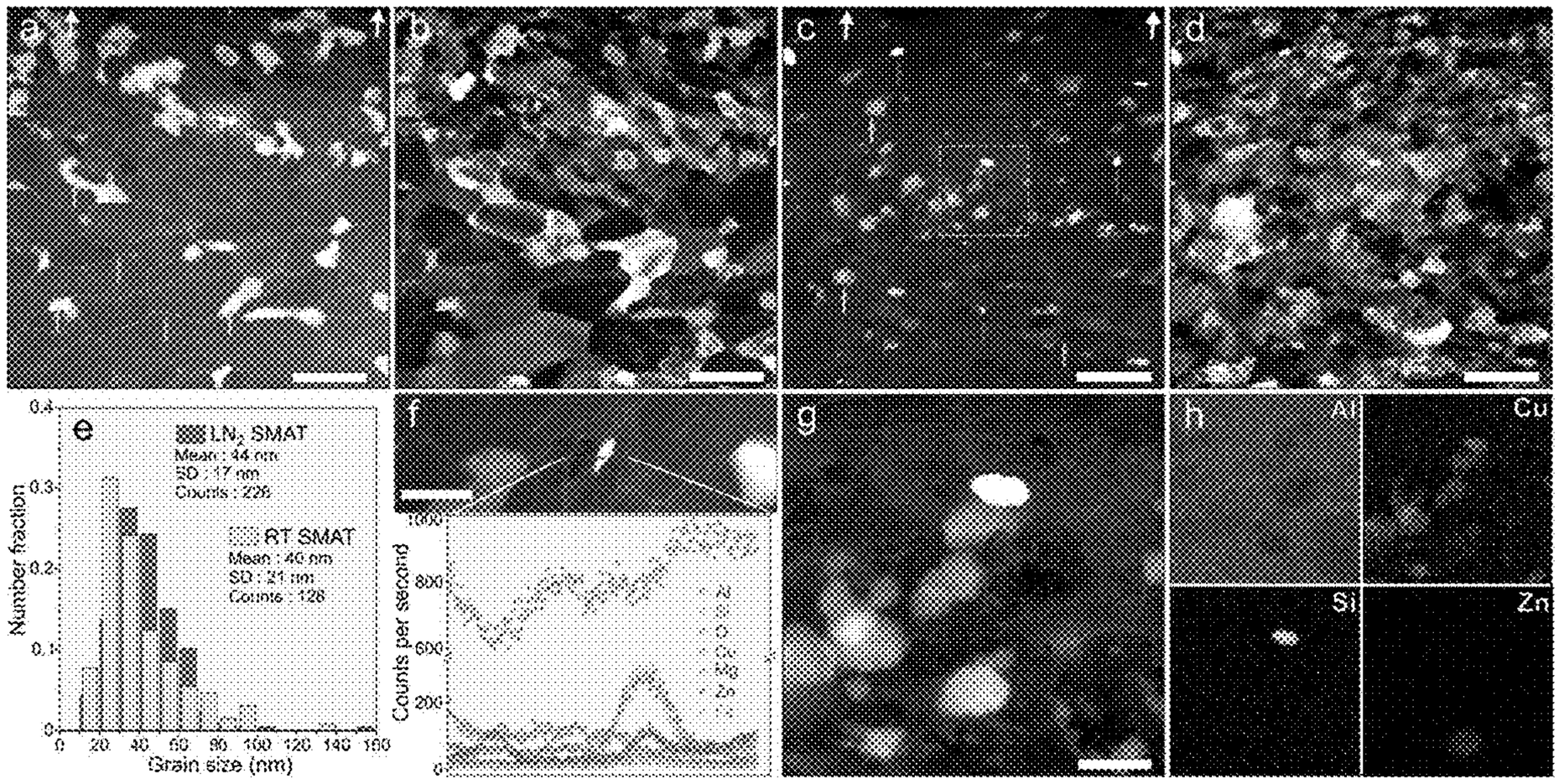
a
b
c
d
e
LN_2 SMAT
Mean : 44 nm
SD : 17 nm
Counts : 229
RT SMAT
Mean : 40 nm
SD : 21 nm
Counts : 128
Number fraction
Grain size (nm)
f
Counts per second
Al
Cu
Mg
Zn
g
h
Al
Cu
Si
Zn

Figure 4

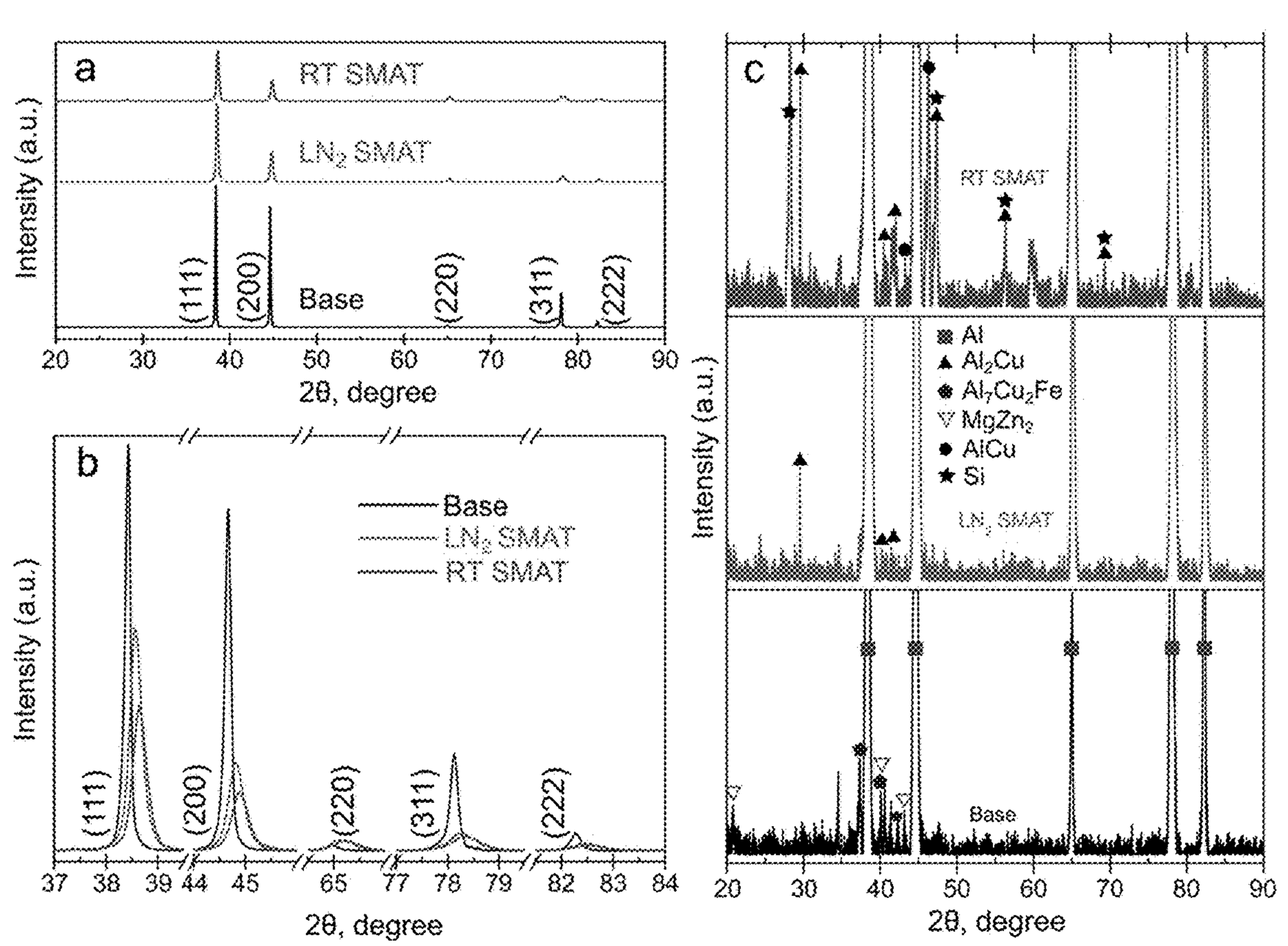
a
RT SMAT
LN2 SMAT
Base
(111)
(200)
(220)
(311)
(222)
Intensity (a.u.)
2θ, degree
b
Base
LN2 SMAT
RT SMAT
c
Al
Al2Cu
Al7Cu2Fe
MgZn2
AlCu
Si

Figure 5

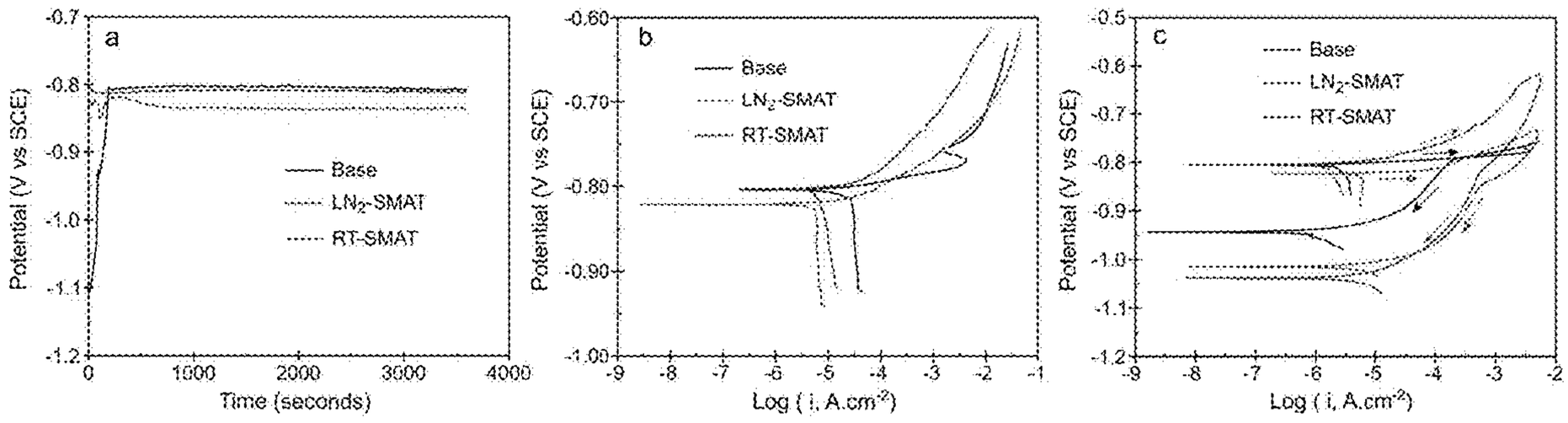
a
Potential (V vs SCE)
Time (seconds)
Base
LN2-SMAT
RT-SMAT
b
Potential (V vs SCE)
Log (i, A.cm-2)
Base
LN2-SMAT
RT-SMAT
c
Potential (V vs SCE)
Log (i, A.cm-2)
Base
LN2-SMAT
RT-SMAT

Figure 6

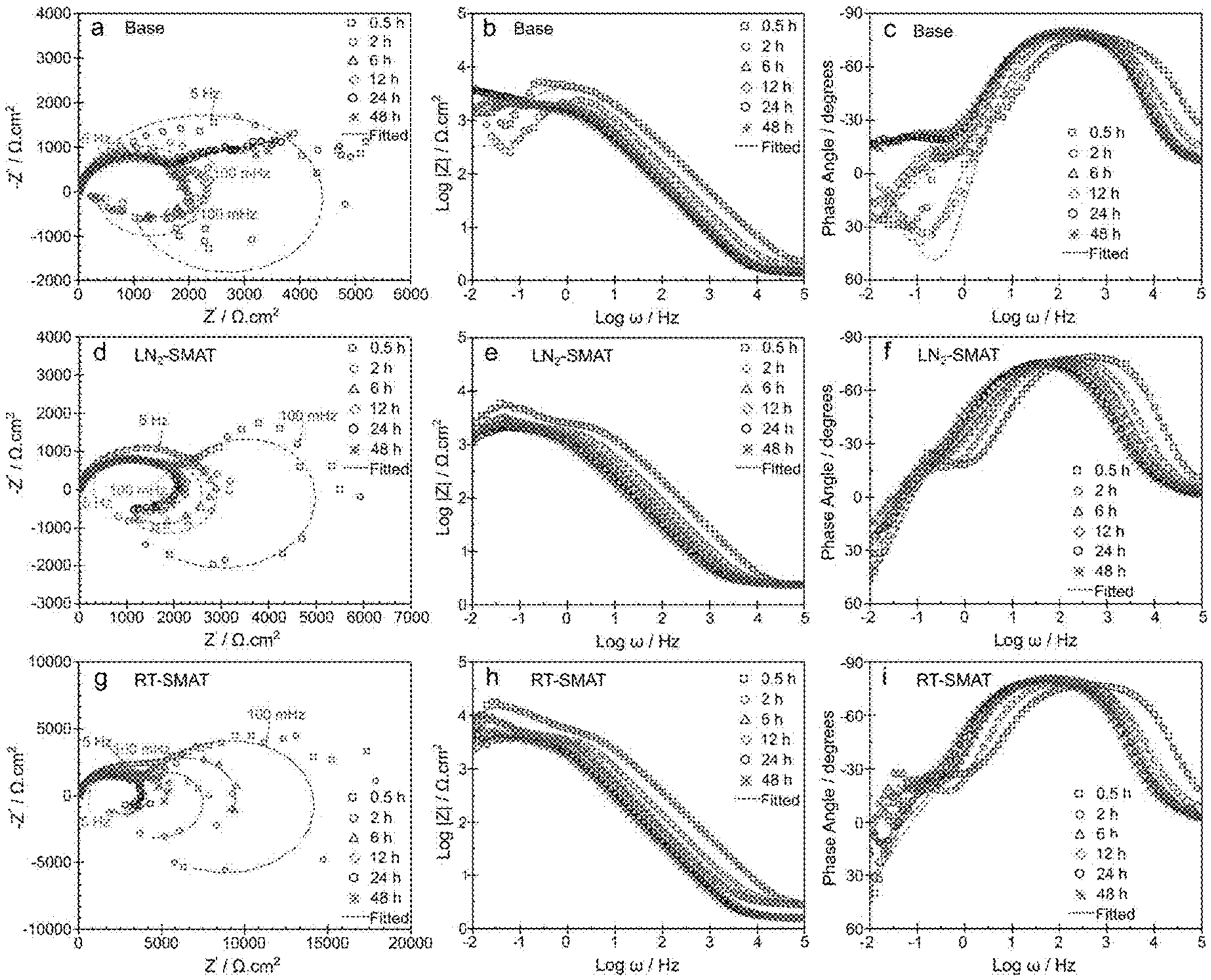
a Base
b Base
c Base
d LN2-SMAT
e LN2-SMAT
f LN2-SMAT
g RT-SMAT
h RT-SMAT
i RT-SMAT
0.5 h
2 h
6 h
12 h
24 h
48 h
Fitted
5 Hz
100 mHz
-Z' / Ω.cm2
Z' / Ω.cm2
Log |Z| / Ω.cm2
Log ω / Hz
Phase Angle / degrees

Figure 7

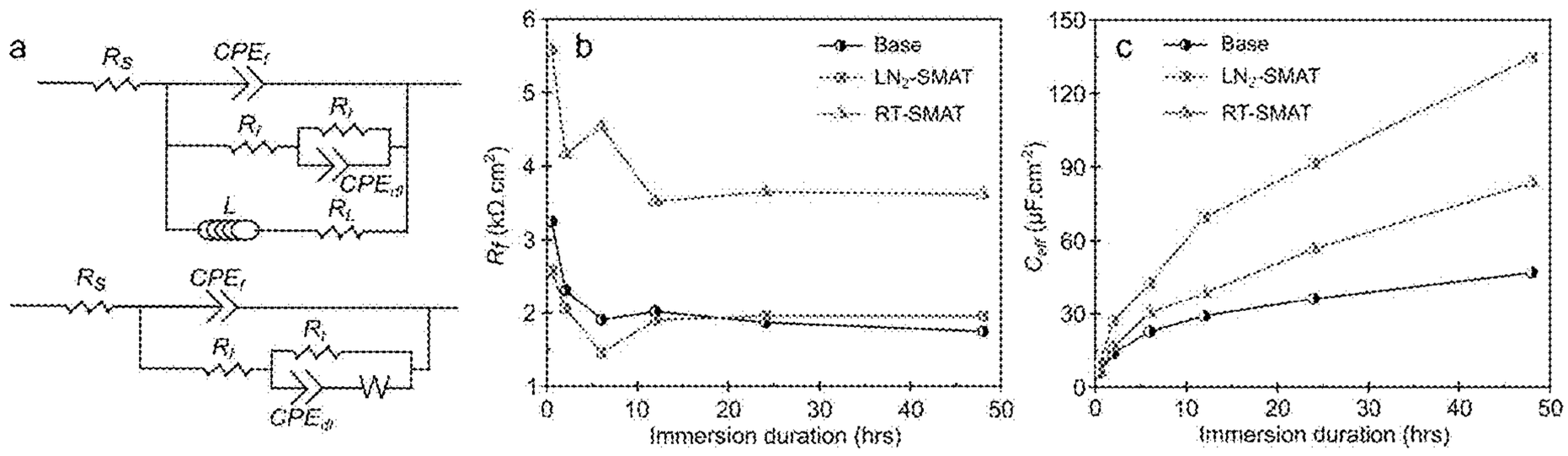
a
R_S
CPE_f
R_f
R_t
CPE_{dl}
L
R_L
b
Base
LN_2-SMAT
RT-SMAT
R_f (kΩ.cm^2)
Immersion duration (hrs)
c
C_{eff} (μF.cm^{-2})

Figure 8

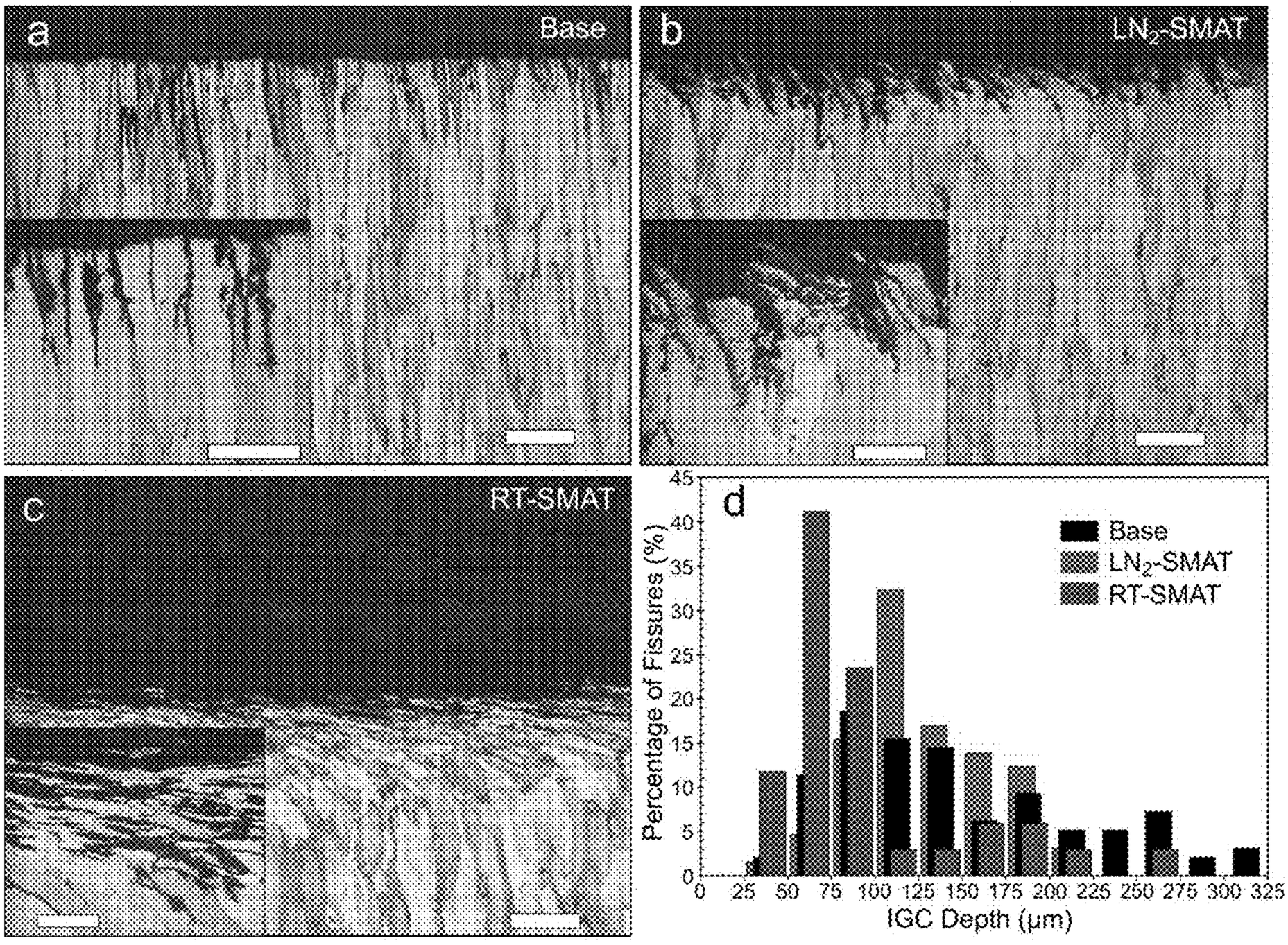
a
Base
b
LN2-SMAT
c
RT-SMAT
d
Base
LN2-SMAT
RT-SMAT
Percentage of Fissures (%)
IGC Depth (μm)
0
5
10
15
20
25
30
35
40
45
0
25
50
75
100
125
150
175
200
225
250
275
300
325

Figure 9

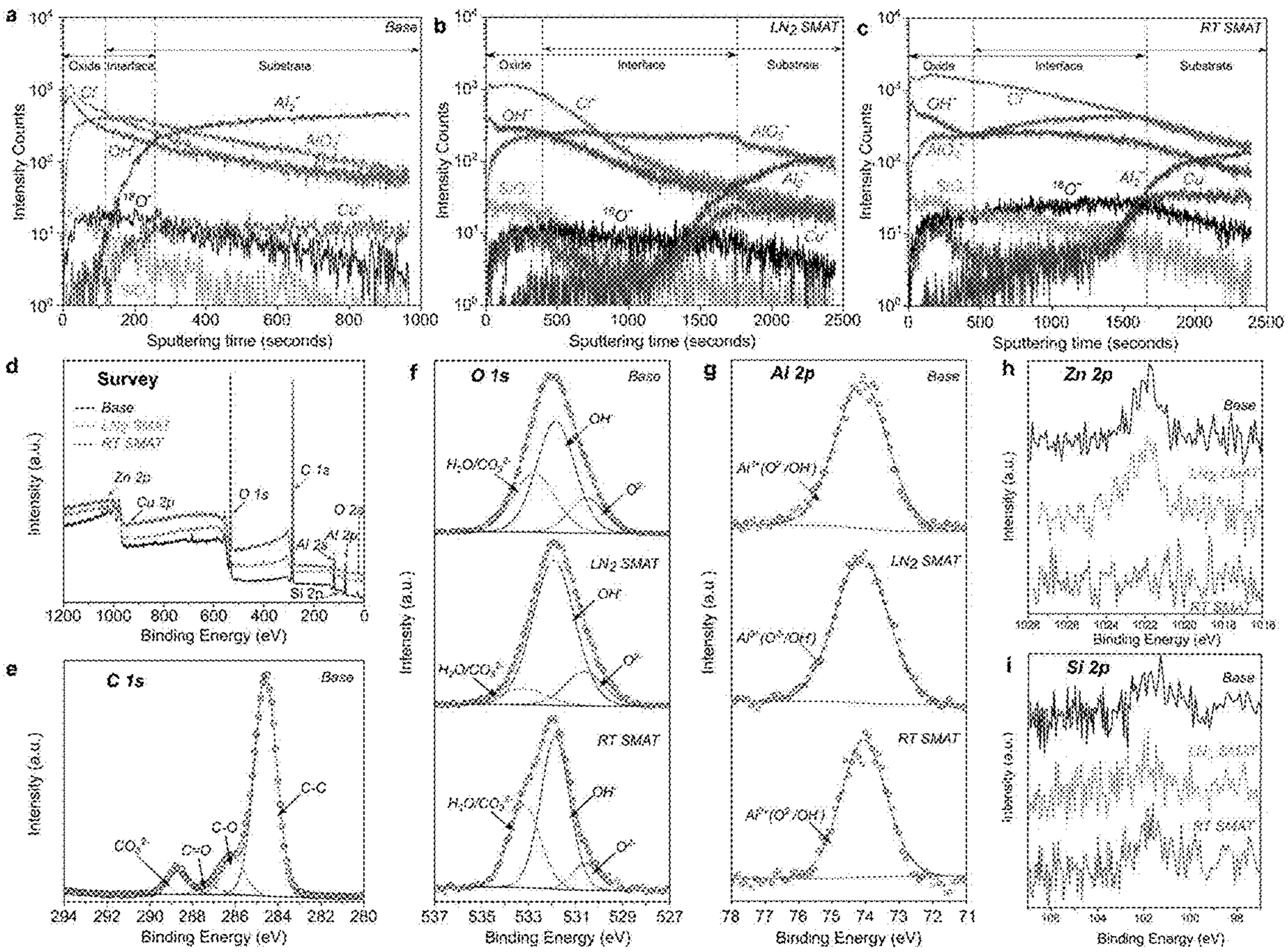
a
Base
Oxide
Interface
Substrate
Intensity Counts
Sputtering time (seconds)
b
LN2 SMAT
c
RT SMAT
d
Survey
Base
LN2 SMAT
RT SMAT
Intensity (a.u.)
Binding Energy (eV)
e
C 1s
f
O 1s
g
Al 2p
h
Zn 2p
i
Si 2p

Figure 10

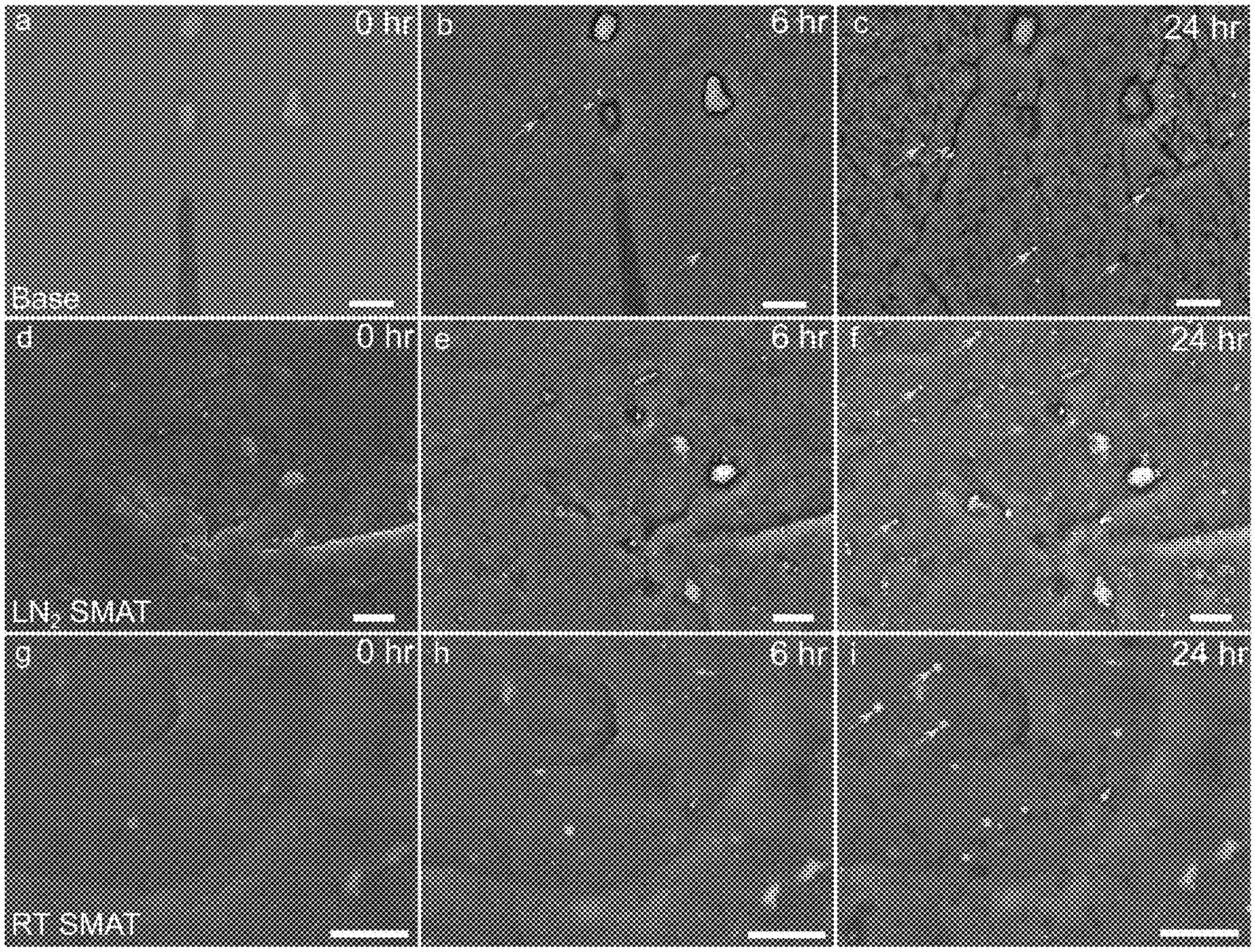
a
0 hr
b
6 hr
c
24 hr
Base
d
0 hr
e
6 hr
f
24 hr
LN2 SMAT
g
0 hr
h
6 hr
i
24 hr
RT SMAT

Figure 11

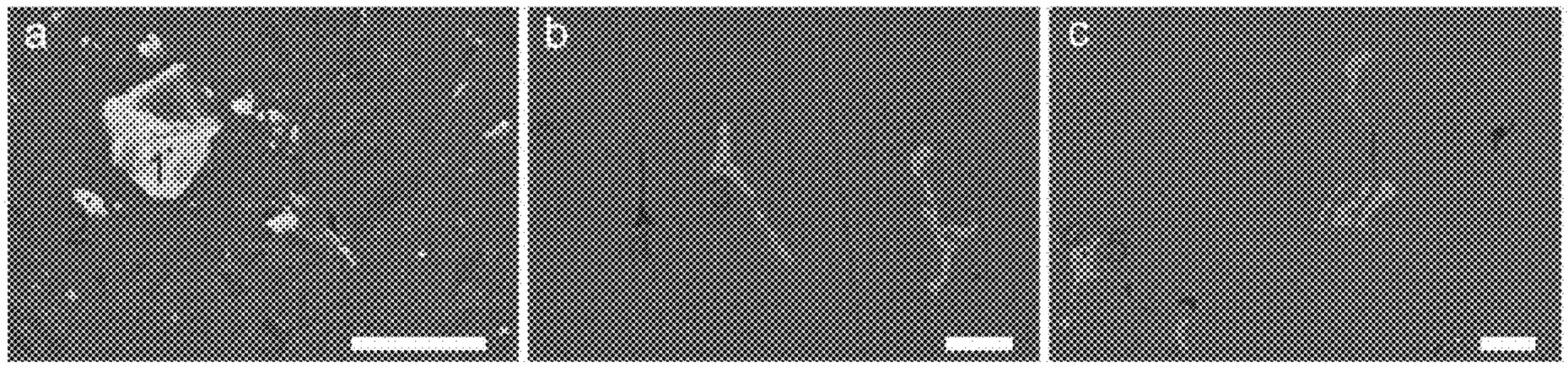

Figure 12

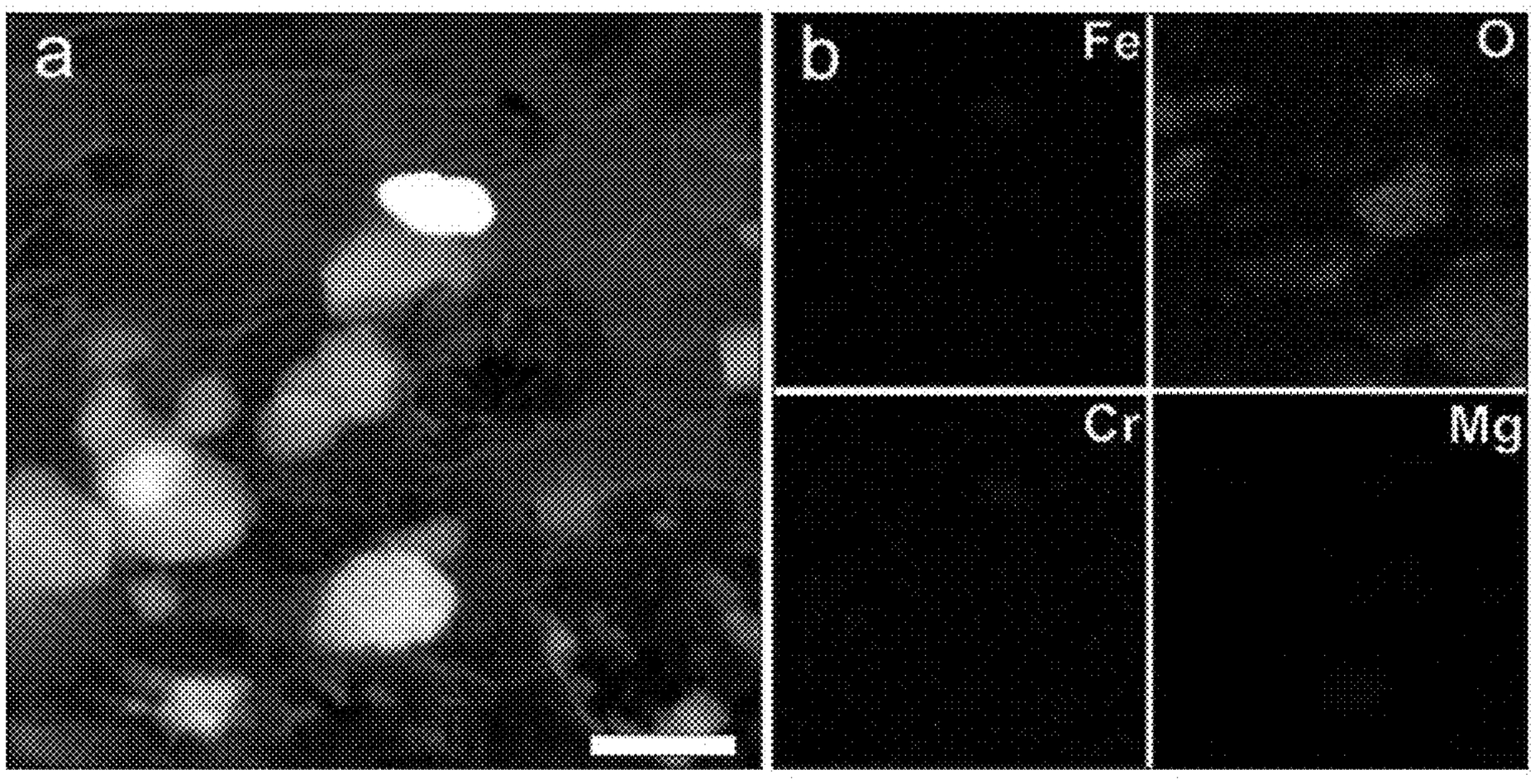

Figure 13

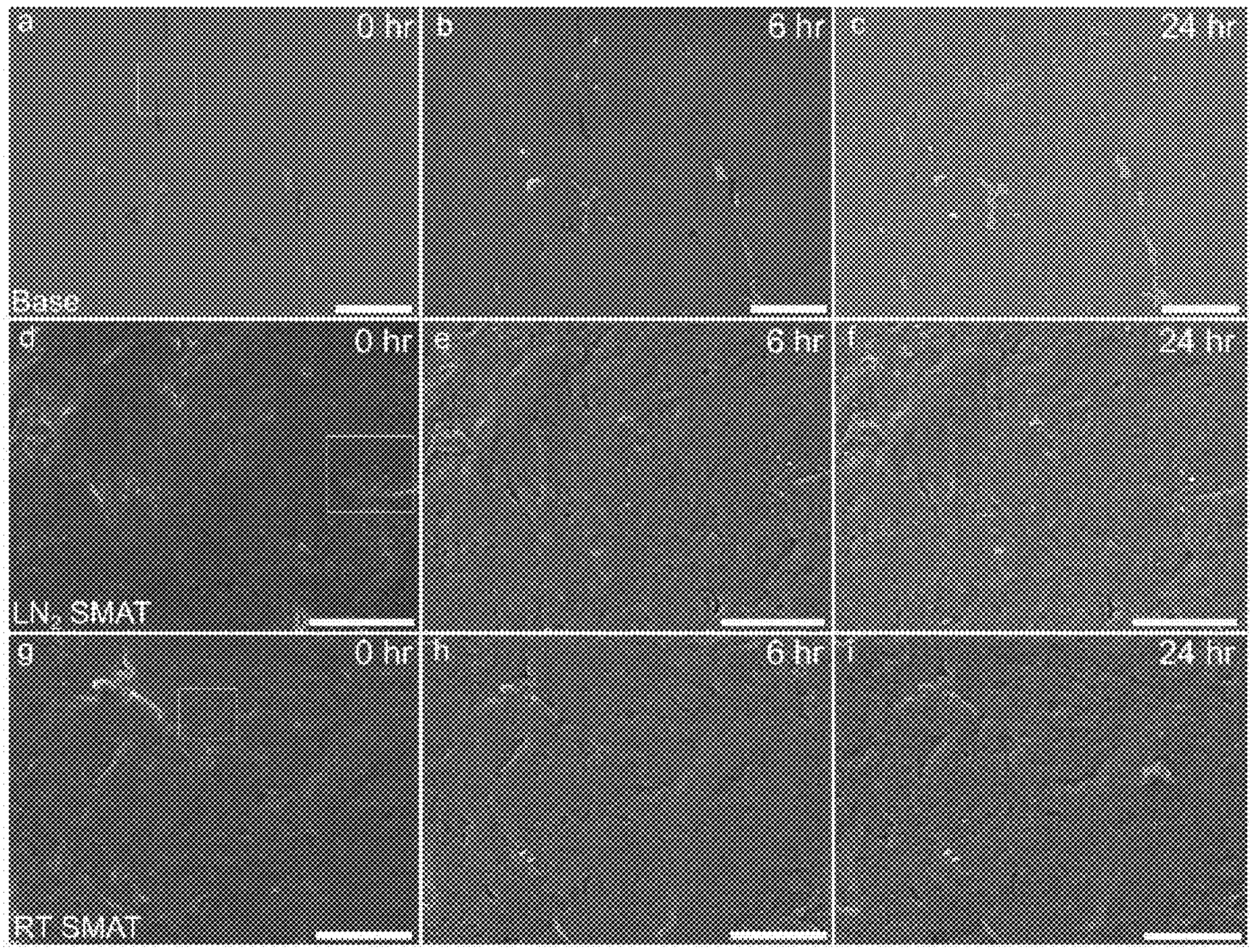
a
0 hr
b
6 hr
c
24 hr
Base
d
0 hr
e
6 hr
f
24 hr
LN2 SMAT
g
0 hr
h
6 hr
i
24 hr
RT SMAT

Figure 14

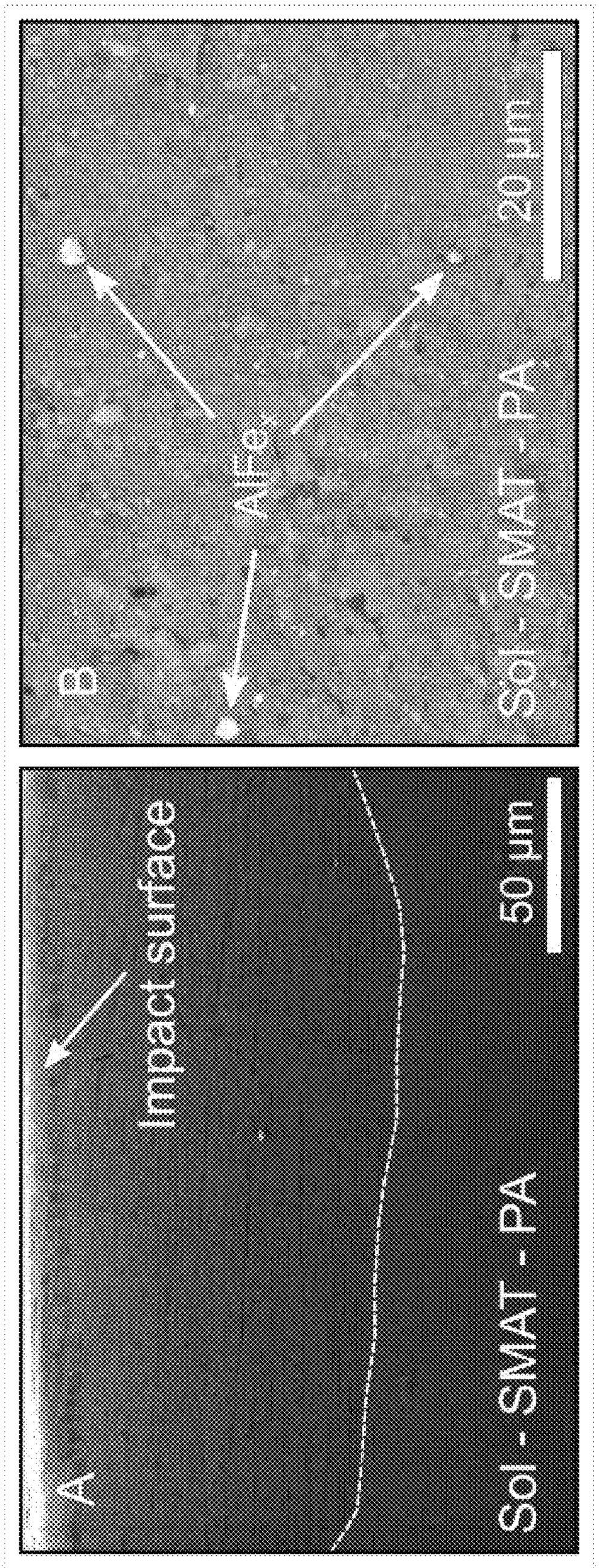

Figure 15

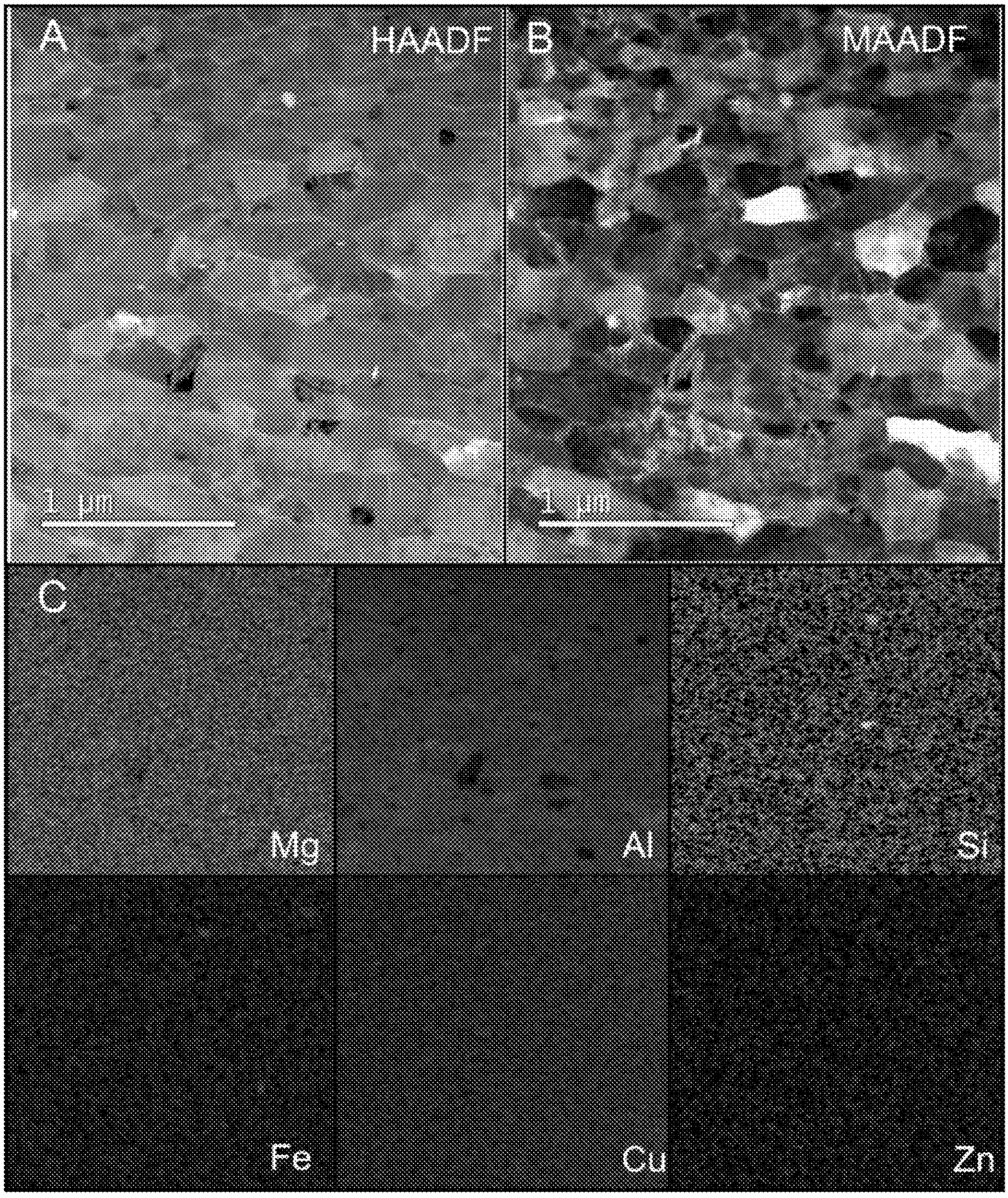

Figure 16

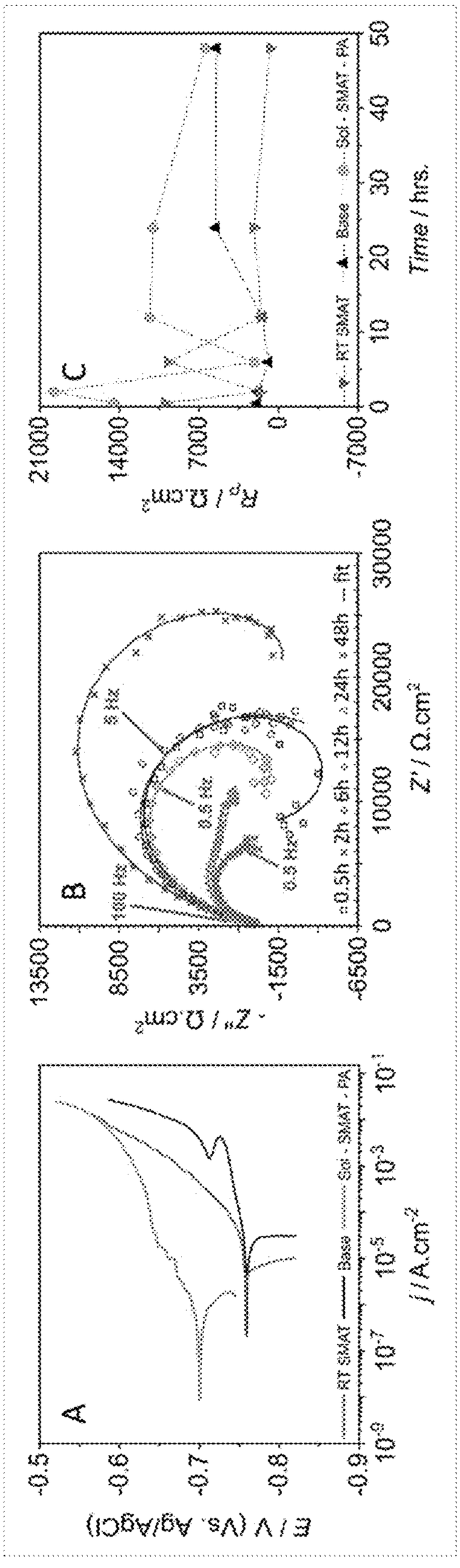
C
RT SMAT
Base
Sol - SMAT - PA
Time / hrs.
B
0.5h
2h
6h
12h
24h
48h
fit
Z'' / Ω.cm²
Z' / Ω.cm²
R_ct / Ω.cm²
A
E / V (vs. Ag/AgCl)
I / A.cm⁻²

Figure 17

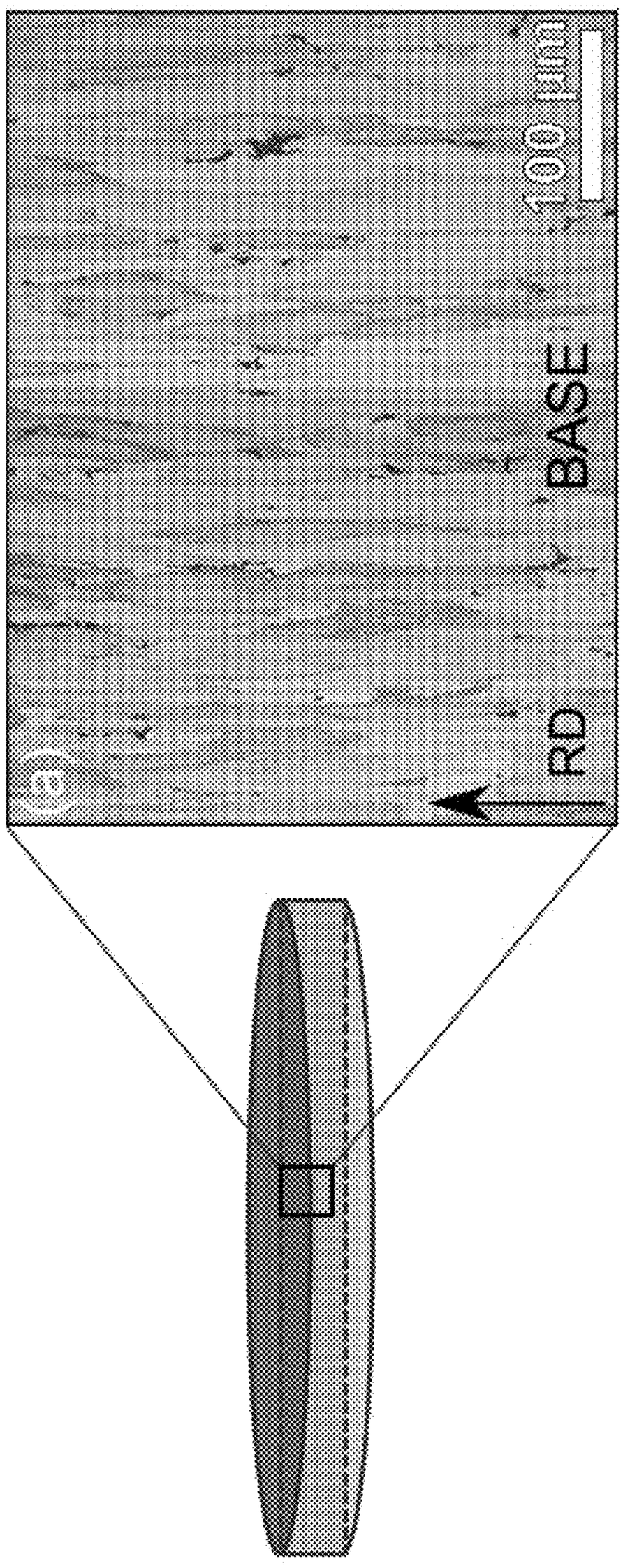

Figure 18

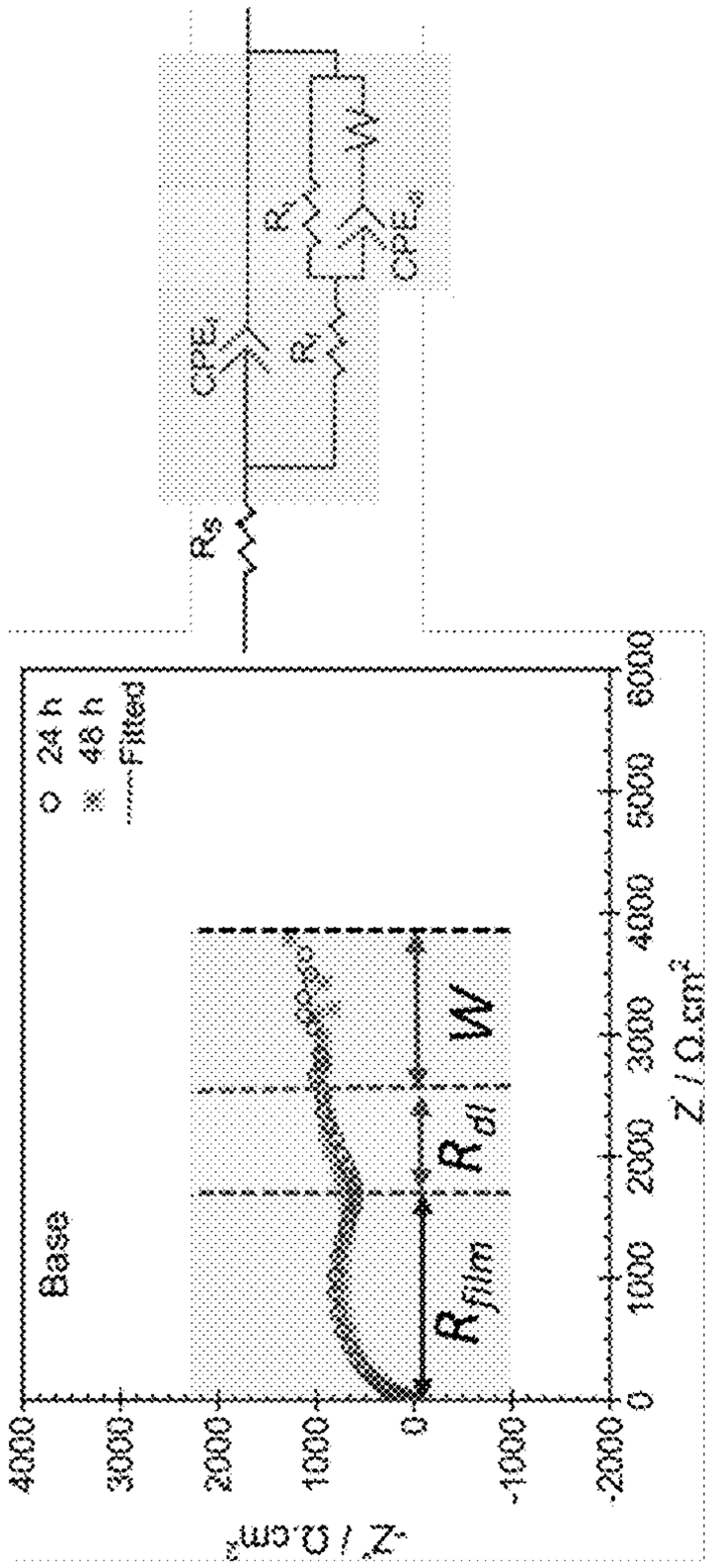
Base
24 h
48 h
Fitted
R_{film}
R_{dl}
W
Z' / Ω.cm²
$-Z''$ / Ω.cm²
4000
3000
2000
1000
0
-1000
-2000
0
1000
2000
3000
4000
5000
6000

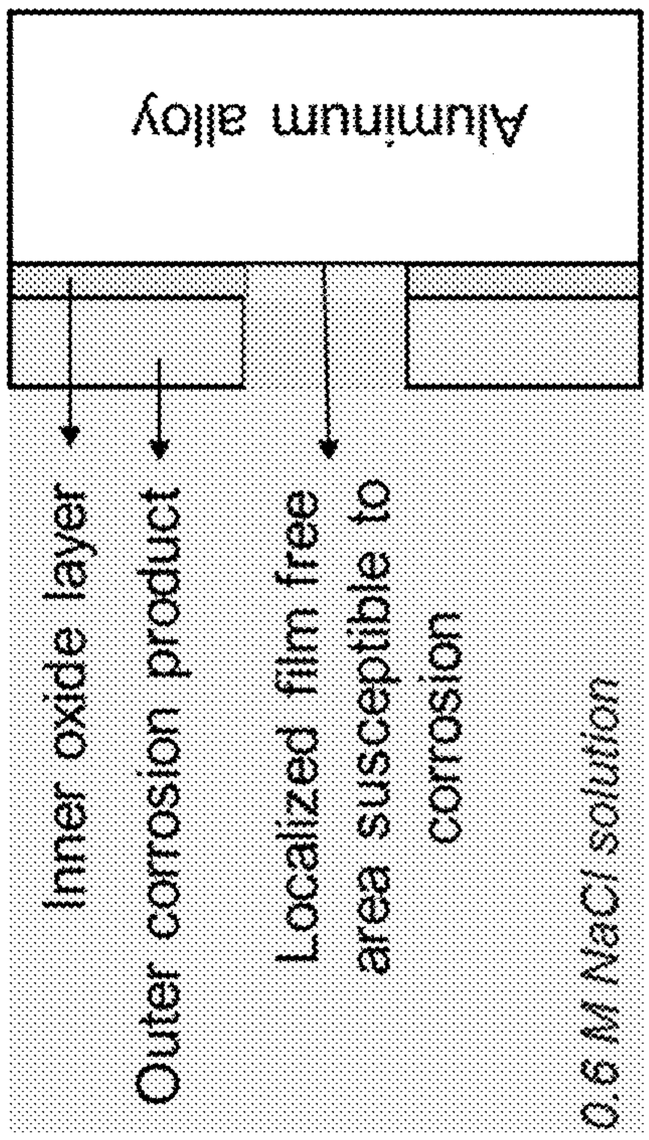
Aluminum alloy
Inner oxide layer
Outer corrosion product
Localized film free area susceptible to corrosion
0.6 M NaCl solution

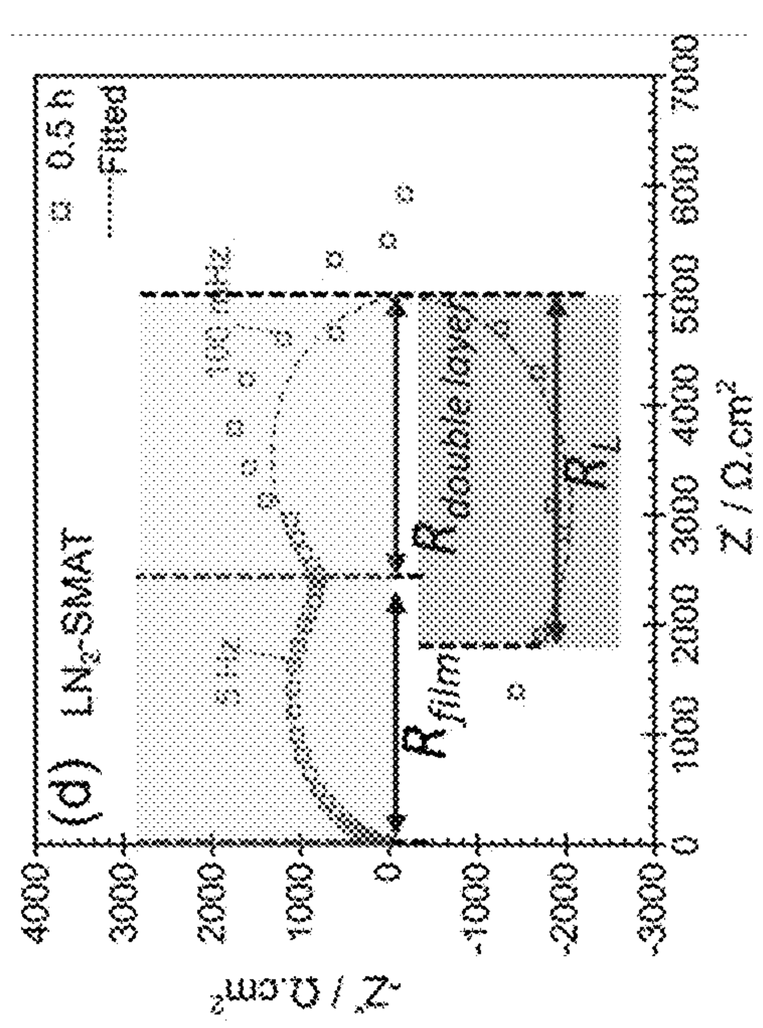
(d) LN$_2$-SMAT
0.5 h
Fitted
R_{film}
$R_{double\ layer}$
R_L
Z' / Ω.cm²
$-Z''$ / Ω.cm²
4000
3000
2000
1000
0
-1000
-2000
-3000
0
1000
2000
3000
4000
5000
6000
7000

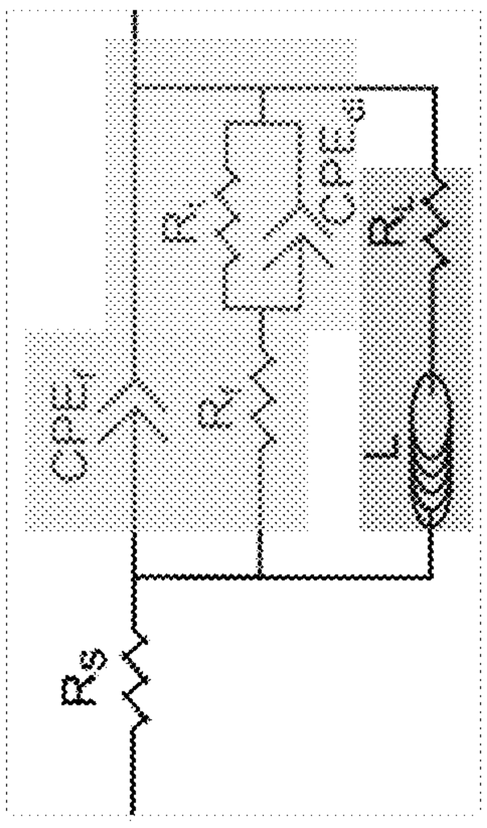
R_S
CPE$_1$
R_1
R_2
CPE$_2$
R_L
L

Figure 19

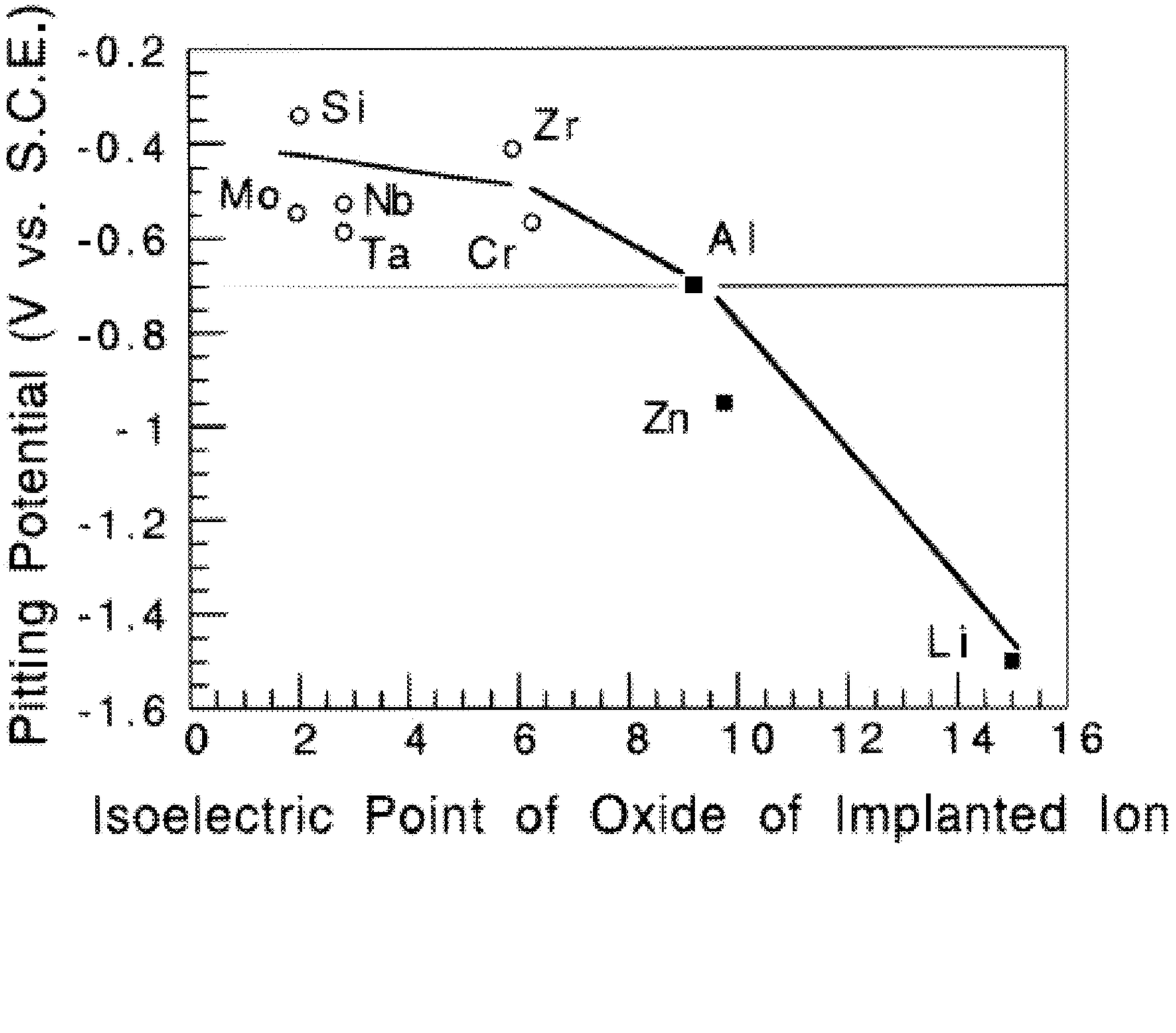
Pitting Potential (V vs. S.C.E
-0.2
-0.4
-0.6
-0.8
-1
-1.2
-1.4
-1.6
Si
Zr
Mo
Nb
Ta
Cr
Al
Zn
Li
0
2
4
6
8
10
12
14
16
Isoelectric Point of Oxide of Implanted Ion

Figure 20

SURFACE ATTRITION TREATMENT, COMPOSITIONS, AND METHODS OF USE THEREOF

GOVERNMENT INTERESTS

[0001] This invention was made with government support under W911NF-15-2-0038 awarded by the Army Research Office. The government has certain rights in the invention.

[0002] This application claims prior to U.S. Provisional Application No. 63/424,041, filed on Nov. 9, 2022, the entire contents of which are incorporated herein by reference.

[0003] All patents, patent applications and publications cited herein are hereby incorporated by reference in their entirety. The disclosures of these publications in their entireties are hereby incorporated by reference into this application in order to more fully describe the state of the art as known to those skilled therein as of the date of the invention described and claimed herein.

FIELD OF THE INVENTION

[0005] The present invention relates to surface attrition treatment, compositions, and methods of use thereof.

BACKGROUND OF THE INVENTION

[0006] Gradient nanostructure (GNS), a class of hetero-structure materials has gained attention in the material community due to its ability to achieve a combination of high strength and ductility without altering the overall alloy composition. These properties are derived from hetero-deformation-induced strengthening and strain-hardening by the synergistic interaction between hard and soft zones. GNS materials have also shown improvement in surface-sensitive properties such as fatigue, wear, corrosion-fatigue, and corrosion behavior of materials. However, there have been limitations on processing of bulk samples with controlled microstructure for mechanical properties.

SUMMARY OF THE INVENTION

[0007] Aspects of the invention are drawn towards a method of producing a gradient nano-grained surface layer on an alloy comprising: obtaining a milling media and a base alloy; coating the milling media in a powder; and subjecting the base alloy to surface mechanical attrition treatment (SMAT) by impacting the alloy with the coated milling media to generate a SMAT alloy with a gradient nano-grained surface layer. In embodiments, the base alloy is subjected to heat treatment or is not subjected to heat treatment. In further embodiments, the heat treatment comprises solutionization, aging treatment, or a combination thereof. In embodiments, the alloy is subjected to heat treatment before SMAT, subjected to heat treatment after SMAT, or subjected to heat treatment both before and after SMAT. In embodiments, the milling media comprises stainless steel. In embodiments, the stainless steel comprises 440C stainless steel. In embodiments, the base alloy comprises an aluminum alloy. In further embodiments, the base alloy comprises 7075 aluminum alloy, 2024 aluminium alloy, 5083 aluminium alloy, and 6061 aluminium alloy. In embodiments, the powder comprises elements which do not induce more cathodic precipitates. In embodiments, the powder comprises a metal found in the base alloy. In embodiments, the metal comprises aluminum. In embodiments, the powder comprises a metal not found in the base alloy, a metal found in the base alloy, an element, a combination of elements, a ceramic powder, carbide, or combination thereof. In embodiments, the metal comprises aluminum, magnesium, magnesium, copper, iron, chromium, titanium, zinc, scandium, vanadium, cobalt, nickel, silicon, or a combination thereof. In embodiments, the surface mechanical attrition treatment (SMAT) is performed at room temperature or liquid-nitrogen (LN_2) cooled temperature. In embodiments, the SMAT alloy has improved corrosion resistance compared to the base alloy. In embodiments, the SMAT alloy has improved surface resistance compared to the base alloy. In some embodiments, the elemental components of the SMAT alloy are not changed compared to the base alloy.

[0008] Aspects of the invention are drawn towards a SMAT alloy produced by any one of the methods described herein. In embodiments, the SMAT alloy has improved corrosion resistance compared to an untreated alloy. In embodiments, the SMAT alloy has improved surface resistance compared to an untreated alloy. In embodiments, the SMAT alloy has a higher thickness of oxide layer compared to an untreated alloy when exposed to a corrosive agent.

[0009] Other objects and advantages of this invention will become readily apparent from the ensuing description.

BRIEF DESCRIPTION OF THE FIGURES

[0010] The patent or application file contains at least one drawing executed in color. Copies of this patent or patent application publication with color drawings will be provided by the Office upon request and payment of necessary fee.

[0011] FIG. **1** shows a schematic of Surface Mechanical Attrition Treatment (SMAT). Panel a coating stainless steel milling media with pure aluminum powder in liquid nitrogen (LN_2) flow environment, Panel b SMAT of aluminum alloy samples in room temperature (RT) and LN_2 flow condition, Panel c schematic showing resulted gradient microstructural changes through SMAT.

[0012] FIG. **2** shows optical micrograph of the cross-sectional surface after SMAT. Panel a Base untreated alloy, Panel b LN_2 SMAT, and c RT SMAT. Scale bars in Panels a, b, and c indicate 100 μm.

[0013] FIG. **3** shows surface microstructure evolution with SMAT. Panel a collage of RT SMAT and LN_2 SMAT surfaces; Backscattered scanning electron micrograph (BSE-SEM) of the top surface and enlarged sections of image FIG. **3** panels a; b LN_2 SMAT, c RT SMAT, and d base; Cross-sectional images of panels e LN_2 SMAT and f RT SMAT. Scale bars in panel a indicate 2 mm; in panels b, c, and d indicate 20 μm and in panels e and f indicate 10 μm.

[0014] FIG. **4** shows STEM characterization of SMAT samples. HAADF and respective MAADF image of panels a-b LN_2 SMAT and panels c-d RT SMAT sample with the white arrow showing the SMAT surface, red, green, and blue arrows indicate Si-based, Cu based phase and heavier element along grain boundaries, panel e grain size distribution for top 500 nm depth from SMAT surfaces, panel f EDS line profile showing composition variation across a dark phase adjacent to a bright phase in LN_2 SMAT sample, panel g

magnified HAADF image from FIG. **4** panels c and h respective EDS elemental mapping image of Al, Cu, Si, and Zn. Scale bars in panels a, b, c, and d indicate 200 nm, and in panels f and g indicate 50 nm.

[0015] FIG. **5** shows XRD characterization of SMAT samples. Panel a X-ray diffraction (XRD) pattern of base untreated, LN_2 SMAT and RT SMAT surfaces; panel b XRD peaks of three surfaces at different pure aluminum hkl planes, which showed peak full width at half maxima (FWHM) broadening and higher angle shift of peak position with SMAT treatment; panel c XRD peaks at low intensity of three surfaces to address the dissolution and formation second phase after SMAT.

[0016] FIG. **6** shows open circuit potential (OCP) and Polarization curves. Panel a OCP measurements; panel b Potentiodynamic polarization and panel c Cyclic potentiodynamic polarization curves after 10 minutes and 30 minutes of immersion in 0.6 M NaCl solution with initial near-neutral pH (6.5±0.2) for base untreated, LN_2 SMAT, and RT SMAT samples, respectively.

[0017] FIG. **7** shows electrochemical impedance spectroscopy (EIS) measurements (scatter plot) and model fit (solid dash line) at different immersion times. Nyquist, bode-bode, and bode-phase angle plots for panels a-c Base untreated; panels d-f LN_2 SMAT; panels g-i RT SMAT.

[0018] FIG. **8** shows a representation of electrochemical parameters derived from EIS. Panel a Equivalent circuits used for fitting EIS curves for different immersion times; panel b variation of surface film resistance with immersion times obtained through EIS curve fitting; and panel c variation of effective capacitance with immersion time calculated by equation (4).

[0019] FIG. **9** shows intergranular corrosion measurements in SMAT samples. Optical micrographs of an etched cross-section of AA7075 alloy after intergranular corrosion test for 24 hours according to ASTM-G110 standard. Panel a Base untreated alloy, panel b LN_2 SMAT alloy, panel c RT SMAT alloy, and panel d A histogram plot comparing intergranular corrosion penetration depth for three alloys. Scale bars in panels a, b, and c indicate 200 μm, and inserts in respective images indicate 100 μm.

[0020] FIG. **10** shows ToF-SIMS and XPS characterization of surface films. ToF-SIMS negative ion depth profile after immersion in 0.6 M NaCl solution for 15 minutes for panel a Base untreated alloy; panel b LN_2 SMAT alloy; and panel c RT SMAT alloy. X-ray photoelectron spectrum for all three samples after immersion in immersion in 0.6 M NaCl solution for 15 minutes; panel d survey spectrum, deconvoluted high-resolution spectrums panel e C 1s, panel f O 1s, panel g Al 2p; high-resolution panel h Zn 2p and panel i Si 2p.

[0021] FIG. **11** shows SEM micrographs for post corrosion surface characterization. Scanning electron micrographs of base panels a-c, LN_2 SMAT panels d-f, and RT SMAT panels g-i alloy after immersion in quiescent 0.6 M NaCl solution for different times (shown in corresponding figures). Red, green, and yellow arrows represent the cathodic phases, precipitates at the grain boundary, and corrosion products, respectively. Scale bars in panels a-i indicate 5 μm.

[0022] FIG. **12** shows SEM micrographs of panel a LN_2 SMAT, panels b & c Base specimens indicating the location of EDS analysis. Scale bars in panels a, b, and c indicate 20 μm.

[0023] FIG. **13** shows panel a magnified HAADF image from FIG. **4** panels c and b respective EDS elemental mapping image of Fe, 0*, Cr, and Mg. Scale bars in panel a indicate 50 nm. *(The presence of oxygen in the EDS map along Al in FIG. **4** panel h suggest that the Al_2O_3 oxide layer formed on the top surface has been fragmented and incorporated with the top nanograin layer during high strain rate deformation by the impact of Al-coated stainless-steel balls).

[0024] FIG. **14** shows scanning electron micrographs of base panels a-c, LN_2 SMAT panels d-f, and RT SMAT panels g-i alloy after immersion in quiescent 0.6 M NaCl solution for different times (shown in corresponding figures). The yellow boxes as inserts represent the location that is further magnified and shown in FIG. **11**. Scale bars in panels a-i indicate 50 μm.

[0025] FIG. **15** shows scanning electron micrograph images of (panel a) cross-section and (panel b) top surface of the Sol-SMAT-PA sample.

[0026] FIG. **16** shows transmission electron micrograph images of the Sol-SMAT-PA sample: (panel a) HAADF, (panel b) MAADF, and (panel c) EDS elemental mapping of constituent elements.

[0027] FIG. **17** shows non-limiting, exemplary electrochemical characterization data: (panel a) Potentiodynamic polarization curves, (panel b) Nyquist plot, (panel c) polarization resistance.

[0028] FIG. **18** shows a non-limiting, representative schematic of locations where optical micrographs of the cross-sectional surface measurements was acquired on a sample.

[0029] FIG. **19** shows a non-limiting, representative schematic of corrosion behaviors as measured by EIS and fitted to an electrical circuit model.

[0030] FIG. **20** shows a non-limiting, exemplary graph of pitting potential versus the isoelectric point of oxide of implanted ion.

DETAILED DESCRIPTION OF THE INVENTION

[0031] Gradient nano-grained structures have been used as a technique to evade the strength-ductility trade-off in metals and alloys. Herein, we describe the effect of surface mechanical attrition treatment (SMAT) on the microstructure and corrosion behavior of the high-strength aluminum alloy. SMAT was performed at room temperature and liquid-nitrogen (LN_2) flow conditions to generate two distinctly different initial gradient microstructures.

[0032] Detailed descriptions of one or more embodiments are provided herein. It is to be understood, however, that the present invention can be embodied in various forms. Therefore, specific details disclosed herein are not to be interpreted as limiting, but rather as a basis for the claims and as a representative basis for teaching one skilled in the art to employ the present invention in any appropriate manner.

[0033] The singular forms "a", "an" and "the" include plural reference unless the context clearly dictates otherwise. The use of the word "a" or "an" when used in conjunction with the term "comprising" in the claims and/or the specification can mean "one," but it is also consistent with the meaning of "one or more," "at least one," and "one or more than one."

[0034] Wherever any of the phrases "for example," "such as," "including" and the like are used herein, the phrase "and without limitation" is understood to follow unless explicitly

stated otherwise. Similarly, "an example," "exemplary" and the like are understood to be nonlimiting.

[0035] The term "substantially" allows for deviations from the descriptor that do not negatively impact the intended purpose. Descriptive terms are understood to be modified by the term "substantially" even if the word "substantially" is not explicitly recited.

[0036] The terms "comprising" and "including" and "having" and "involving" (and similarly "comprises", "includes," "has," and "involves") and the like are used interchangeably and have the same meaning. Specifically, each of the terms is defined consistent with the common United States patent law definition of "comprising" and is therefore interpreted to be an open term meaning "at least the following," and is also interpreted not to exclude additional features, limitations, aspects, etc. Thus, for example, "a process involving steps a, b, and c" means that the process includes at least steps a, b and c. Wherever the terms "a" or "an" are used, "one or more" is understood, unless such interpretation is nonsensical in context.

[0037] As used herein, the term "about" can refer to approximately, roughly, around, or in the region of. When the term "about" is used in conjunction with a numerical range, it modifies that range by extending the boundaries above and below the numerical values set forth. In general, the term "about" is used herein to modify a numerical value above and below the stated value by a variance of 20 percent up or down (higher or lower).

[0038] As used herein, the term "substantially the same" or "substantially" can refer to variability typical for a particular method is taken into account.

[0039] The terms "sufficient" and "effective", as used interchangeably herein, can refer to an amount (e.g., mass, volume, dosage, concentration, and/or time period) needed to achieve one or more desired result(s).

[0040] Before explaining at least one embodiment of the disclosure in detail, it is to be understood that the disclosure is not necessarily limited in its application to the details set forth in the following description or exemplified by the examples. The disclosure is capable of other embodiments or of being practiced or carried out in various ways. Other compositions, compounds, methods, features, and advantages of the present disclosure will be or become apparent to one having ordinary skill in the art upon examination of the following drawings, detailed description, and examples. All such additional compositions, compounds, methods, features, and advantages can be included within this description, and be within the scope of the present disclosure.

[0041] Methods of Producing Gradient Nano-Grained Surface Layer

[0042] Aspects of the invention are drawing towards methods of producing a gradient nano-grained surface layer on an alloy. As used herein, the term "alloy" can refer to a material comprising a base element and one or more intentional alloying adducts. In embodiments, the alloy can comprise impurities. For example, the alloy can comprise a mixture of chemical elements wherein at least one element is a metal. As used herein the term "base element" can refer to the element that is the main constituent of an alloy. As used herein, the term "base alloy" can refer to the alloy that is to undergo further modified. For example, the modification can comprise surface treatment. In embodiments, the surface treatment comprises surface mechanical attrition treatment (SMAT). SMAT can refer to a method for the refinement of the surface grain structure of a material.

[0043] In embodiments, the method of producing a gradient nano-grained surface layer on an alloy can comprise obtaining a milling media and a base alloy, coating the milling media in a metal powder, and subjecting base alloy to surface mechanical attrition treatment (SMAT) by impacting the alloy with the coated milling media to generate a SMAT alloy with a gradient nano-grained surface layer. In some embodiments, the alloy can be heat treated prior to being subjected to SMAT, after being subjected to SMAT, or both before and after being subjected to SMAT. For example, performing heat treatment before SMAT can provide the last step (SMAT) to fragment and/or dissolve the inherent second phase particles and dynamic precipitation of metastable phases (i.e., pure Si, pure Zn, Al_2Cu in aluminium 7075 alloy). In embodiments, the alloy can be subjected to heat treatment before SMAT, after SMAT, or both before and after SMAT. For example, performing heat treatment after SMAT can allow the super saturated solid solution created during SMAT to be utilized for the controlled precipitation of nanoscale precipitates. In embodiments, the benefits of heat treating before or after SMAT can depend on the type of second phase formed.

[0044] In embodiments, the heat treatment can enhance strength. For example, the heat treatment can comprise subjecting an alloy to solutionization, aging treatment, or a combination thereof. As used herein, the term "solutionization" or "solutionizing" can refer to solution heat treating and quenching. For example, the alloy can be heated to a suitable temperature for a period of time to allow for soluble elements to enter solid solution. For example, the suitable temperature can comprise about the solvus temperature. For example, the suitable temperature can comprise above the solvus temperature or below the solvus temperature. In embodiments, the quenching can comprise cooling the solution rapidly enough to hold the elements in a solid solution.

[0045] As used herein, the term "aged" or "aging treatment" can refer to a process of heating the alloy to produce precipitates. In embodiments, the base alloy can be in peak age condition. As used herein, the term "peak age condition" can refer to an alloy that has undergone heat treatment to produce nano-scale precipitates and possesses maximum or about maximum mechanical properties.

[0046] In some embodiments, the alloy can be solutionized prior to SMAT and aged after SMAT. As used herein, the term "sol-SMAT-PA" can refer to the process of subjecting an alloy to solutionization, then subjecting the alloy to SMAT, and finally, subjecting the alloy to aging treatment. For example, the heat treatment can comprise subjecting an aluminum alloy to a temperature of about 475° C. for about 2 hours, quenching the alloy with water, subjecting the quenched alloy to a temperature of about 120° C. for about 24 hours, and furnace cooling the alloy.

[0047] In some embodiments, the alloy can be subjected to heat treatment before SMAT. For example, the alloy can be solutionized, subjected to aging, and then subjected to SMAT. For example, the heat treatment can comprise subjecting an aluminum alloy to a temperature of about 475° C. for about 2 hours, quenching the alloy with water, subjecting the quenched alloy to a temperature of about 120° C. for about 24 hours, furnace cooling the alloy, and then subjecting the alloy to SMAT.

[0048] As used herein the term "corrosion" can refer to the degradation of a material caused by its environment. For example, corrosion can refer to the degradation of properties of a metal or metal alloy due to reaction with its surroundings. As used herein, the phrase "increased corrosion properties" can refer to a metal or metal alloy's ability to resist corrosion. For example, the corrosion properties of the alloy after the SMAT method described herein are increased compared to the alloy prior to the SMAT treatment method described herein.

[0049] In embodiments, the base alloy can comprise a metallic alloy. For example, the base alloy comprises can comprise an aluminum alloy, iron alloy, nickel alloy, magnesium alloy, or a combination thereof. For example, the alloy is an aluminum-based alloy, an iron-based alloy, a magnesium-based alloy, or a combination thereof. For example, the aluminum alloy can comprise a 1000 series alloy, a 2000 series alloy, a 3000 series alloy, a 4000 series alloy, a 5000 series alloy, a 6000 series alloy, a 7000 series alloy, a mixed alloy, a cast alloy, or a combination thereof. For example, the aluminum alloy can comprise 7075 aluminum alloy, 2024 aluminium alloy, 5083 aluminium alloy, and 6061 aluminium alloy. Herein, alloys can be referred using International Alloy Designation System, Unified numbering system, or any alloy designation system known in the art.

[0050] As used herein, the term "milling media" can refer to a substance that is used to mill, grind, or crush a material. For example, the milling media can comprise spherical milling media. In embodiments, the spherical milling media can comprise different sizes. In embodiments, the milling media can comprise stainless steel, agate, tungsten carbide, alumina, zirconia, or a combination thereof. In embodiments, the milling media can comprise a material that has higher strength and/or hardness compared to the base alloy. For example, the milling media can comprise stainless steel balls and ceramic milling balls. For example, the milling media comprises a 400 series stainless steel. For example, the milling media comprises 440C stainless steel.

[0051] In embodiments, the milling media is coated in a powder prior to subjecting the base alloy to SMAT. In some embodiments, the powder comprises elements and/or compositions which does not lower the corrosion resistance. For example, the powder does not induce more cathodic precipitates or particles. For example, the powder can comprise a metal powder. Without wishing to be bound by theory, the metal powder coating can prevent contamination from the milling media into the base alloy. In embodiments, the metal powder can comprise a metal found in the base alloy, or a metal not found in the base alloy. In some embodiment, the powder comprises metal, one or more elements, ceramics, carbides, or a combination thereof.

[0052] In some embodiments, the milling media is coated in a metal powder that is found in the base alloy. For example, if the base alloy is an aluminum alloy, the milling media can be coated in aluminum powder. For example, the if the base alloy is a magnesium alloy, the milling media can be coated in magnesium powder. In some embodiments, the metal powder can comprise aluminum, magnesium, copper, iron, chromium, titanium, zinc, scandium, vanadium, cobalt, nickel, silicon, or a combination thereof.

[0053] In some embodiments the metal powder can comprise a metal not found in the base alloy. In some embodiments, coating milling media with a metal powder not found in base alloy can be advantageous. For example, if the metal is noble and corrosion resistant to base alloy and can form a continuous coating without discontinuity after reacting with base alloy. For example, coating Al powder on Mg base alloy. For example, coating with a metal powder that is less corrosion resistant than base alloy and can act as a sacrificial coating. For example, Zn powder on an Al alloy. For example, coating with powder that can form a thicker and coherent oxide layer and have a similar electrochemical potential compared to base alloy. As used herein, the term "coherent" can refer to reduced porosity. For example, Cr powder on an Fe base alloy. In embodiments, the metal not found in the base alloy can comprise aluminum, magnesium, copper, iron, chromium, titanium, zinc, scandium, vanadium, cobalt, nickel, silicon, or a combination thereof. In some embodiments, the metal powder can comprise 1, 2, 3, 4, 5, 6, 7, 8, 9, 10, or more than 10 different metals than what is in the base alloy. In some embodiments, the combination of metal powders can comprise equal proportions or non-equal proportions.

[0054] In embodiments SMAT methods described herein can be performed at about room temperature (RT), about liquid-nitrogen (LN_2) cooled temperature, or any temperature in between. In embodiments, room temperature can comprise about 10° C., about 15° C., about 20° C., about 25° C., about 30° C., about 35° C., about 40° C., about 50° C., about 60° C., about 70° C., or above. In embodiments LN_2 cooled temperature can comprise about −80° C., about −90° C., about −100° C., about −110° C., about −120° C., about −130° C., about −140° C., about −150° C., about −160° C., about −170° C., about −180° C., about −190° C., about −198.2° C., about −200° C., about −210° C., about −220° C., about −230° C., about −240° C., about −250° C., or below.

[0055] As used herein, the term "SMAT alloy" and "SMAT processed alloy" can be used interchangeably. As used herein, the term "SMAT alloy" can refer to an alloy that has been subjected to the SMAT methods as described herein.

[0056] Without wishing to be bound by theory, after subjecting a metal or alloy to the methods described herein, the SMAT alloy can have improved corrosion resistance compared to the base alloy. In embodiments, the SMAT alloy can have improved surface resistance compared to the base alloy. In some embodiments, the elemental components of the SMAT alloy are not changed compared to the base alloy.

[0057] Compositions

[0058] Aspects of the invention are drawn towards compositions made by the methods described herein. For example, the invention comprises an alloy or metal that has been subjected to the methods described herein. For example, the SMAT alloys generated by the methods described herein have improved resistance compared to an untreated alloy. For example, the SMAT alloy has improved surface resistance compared to an untreated alloy. For example, the SMAT alloys described herein have higher thickness of oxide layer compared to an untreated alloy when exposed to a corrosive agent. For example, the SMAT processes described herein can produce a continuous, thick oxide layer which can protect the surface from further corrosion.

[0059] In embodiments, the base alloy thickness can comprise less than 1 nm, about 1 nm, about 5 nm, about 10 nm, or about 15 nm. In embodiments, the SMAT treated alloy

oxide layer thickness can comprise about 15 nm, about 20 nm, about 25 nm, about 30 nm, about 35 nm, about 40 nm, about 50 nm, about 55 nm, about 60 nm, about 65 nm, about 70 nm, about 75 nm, about 80 nm, about 85 nm, about 90 nm, about 95 nm, about 100 nm, or above 100 nm.

EXAMPLES

[0060] Examples are provided below to facilitate a more complete understanding of the invention. The following examples illustrate the exemplary modes of making and practicing the invention. However, the scope of the invention is not limited to specific embodiments disclosed in these Examples, which are for purposes of illustration only, since alternative methods can be utilized to obtain similar results.

Example 1

[0061] Role of Gradient Nanograined Surface Layer on Corrosion Behavior of Aluminum 7075 Alloy

[0062] Abstract

[0063] Gradient nano-grained structures have been a technique to evade the strength-ductility trade-off in metals and alloys. Therefore, in this work, the effect of surface mechanical attrition treatment (SMAT) on the microstructure and corrosion behavior of the high-strength aluminum alloy was investigated. SMAT was performed at room temperature and liquid-nitrogen (LN_2) flow conditions to generate two different initial gradient microstructures. Potentiodynamic polarization, electrochemical impedance spectroscopy, and intergranular corrosion tests were performed. Surface film characterization of untreated and treated samples was performed using X-ray photoelectron spectroscopy and time of flight secondary ion mass spectroscopy techniques. Result reveals significant microstructural changes in SMAT processed samples such as the formation of precipitates and dissolution of inherent phases. In addition, a reduced anodic dissolution rate was observed with the SMAT processed samples. Furthermore, the surface film characterization revealed a thicker oxide film with Cu and SiO_2 enrichment in SMAT samples.

INTRODUCTION

[0064] Gradient nanostructure (GNS), a class of heterostructure materials has gained considerable attention in the material community due to its ability to achieve a combination of high strength and ductility without altering the overall alloy composition[1-4]. These properties are derived from hetero-deformation-induced strengthening and strain-hardening by the synergistic interaction between hard and soft zones[5,6]. GNS materials have also shown improvement in surface-sensitive properties such as fatigue, wear, corrosion-fatigue, and corrosion behavior of materials[7-10]. Besides several advantages, the applicability of these materials hasn't reached its potential due to limitations in the processing of bulk samples with controlled microstructure for mechanical properties[6,10,11].

[0065] Gradient nano-grained structure, as its name indicates, comprises a surface structure of nanocrystalline grains whose magnitude in size gradually increases the further from the surface you are. For example, surface nanocrystallization (SNC) with the nanograins at the surface can be achieved through various severe plastic deformation techniques such as surface mechanical attrition treatment (SMAT)[12], ultrasonic shot peening (USSP)[13], sandblasting[14], laser shock peening (LSP)[15], and fast multiple rotations rolling (FMRR)[16]. Among these SMAT is efficient at producing the smallest grain size at the free surface and an appreciable gradient several hundred microns deep into the bulk of the sample. This gradient forms as a result of dynamic Hertzian impacts of milling media with the sample's free surface which induce a cumulatively high strain value. Generally, the milling media utilized during SMAT are composed of different chemistry than the underlying sample to be processed[17]. The physics and nature of the impacts occur millions of times over thus introducing a way to transfer material. That is the repetitive high rate impacts and local elevation in temperature provide an environment in which atomic diffusion coefficients and chemical reactivity are enhanced facilitating the creation of alloys at the free surface of the sample. If engineered properly the high reactivity of the surface layer and easy diffusion of alloying elements through the grain boundaries of nanograins provides an efficient way to create a corrosion-resistant coating with favorable microstructure[12,18]. For instance, the temperature at which SMAT is carried out can have effects on the degree of grain refinement that occurs at the free surface as well as the depth of gradient formed[19-23]. This has also been found to be true regarding the degree of contaminant and its mixing with the base material. For example, SMAT at cryogenic temperature has shown a higher grain size reduction in pure copper due to a change in underlying deformation mode[19]. Aside from cryo-SNC, alloys prepared through other cryogenic thermo-mechanical processing such as cryo-rolling[24] and cryo-extrusion[25] have shown improved strength as well as ductility compared to their room-temperature processed counterparts. The SMAT processing has been carried out in a university setting on small-scaled simplified geometries such as flat plates. However, modified versions of SMAT processing equipment utilizing acoustic vibrations versus the traditional shaking of changes are allowing SMAT to be applied to tubes/cylinders and even thin wires[9,26,27]. Other embodiments of SMAT processing equipment have employed using burnishing techniques mounted to computer numerical controlled (CNC) machines to allow greater flexibility[2,28,29]. While industrial systems such as the MELD® technology[30] have been developed to tackle the larger scale and more complex parts, the integration of such technology is still in its infant stages in industrial applications.

[0066] The corrosion behavior of nanostructured surfaces obtained through severe plastic deformation (SPD) and surface severe plastic deformation (S^2PD) techniques have been studied in many systems, including aluminum alloys[31-34] pure magnesium, and magnesium alloys[11,35], titanium[36], and stainless steels[8,37,38]. In the case of aluminum alloy, the use of stainless steel balls as a milling medium has been found to contaminate the nanocrystalline layer with iron. Given the galvanic potential difference between the two, the presence of Fe contamination significantly reduced the overall corrosion resistance[34,39]. Similar to aluminum alloys, pure magnesium and magnesium alloys also suffer from impurity contaminations and degradation in corrosion resistance with steel medium-based SMAT processing[35,40]. However, in comparatively harder alloys such as stainless steel and titanium-based alloys, where contamination is minimized, SMAT has been found to enhance corrosion resistance through the creation of a nano-grained surface layer[41-43] within the bulk. A high density of grain boundary

and triple junctions formed within the nano-grained surface was found to significantly enhance the diffusion of chromium to the surface layer in stainless steel. In titanium, processed in a similar manner, this same surface structure allowed oxygen to diffuse into the bulk enhancing the thickness of the oxide layer. In light alloys, in which contamination is more favorable during SMAT, contamination of the surface layer can be avoided by coating the milling medium with non-deleterious elements in order to facilitate its transference to the bulk. Studies have been performed to coat metallic alloys through SMAT-based mechanical alloying[44,45]. In the case of aluminum 2024 and pure aluminum coated with Ni powder, second phases such as Ni_3Al, Al_3Ni, and NiAl were formed on the SMAT surface[46,47]. More such studies have been performed on other systems such as Al coated on steel[48], Ti and Al coated on Ti plates[49] and Al coated on magnesium alloys[45]. In each study, the driving force for easy atomic diffusion in defects and grain boundaries and temperature evolution during SMAT were exploited to form intermetallic compounds and coating on the surface. The morphology and thickness of the coating layer can be tuned by controlling process parameters such as impact energy, milling time, and temperature. No study has been performed with a detailed investigation of SMAT-induced inherent second phases dissolution, precipitation of second phases, and their respective corrosion response in an aluminum alloy.

[0067] Herein, we describe a high-strength aluminum alloy AA7075 that is used for SMAT processing with Al-coated stainless steel balls (FIG. **1**). The SMAT was performed at the room as well as liquid-nitrogen (LN_2) temperature, (samples can be referred to as RT SMAT and LN_2 SMAT herein). A combination of microstructural characterization, electrochemical measurements, and surface spectroscopy characterizations were used to investigate the underlying governing mechanism. The understanding gained through this work indicates a route to improvement of corrosion-resistant aluminum alloys for structural applications in the automotive and aerospace sectors.

[0068] Results

[0069] Microstructure Evolution Through SMAT

[0070] Prior to SMAT, the optical micrograph of the cross-sectional surface shows a rolled microstructure with elongated lamellar grains parallel to rolling directions (FIG. **2** panel a). After SMAT at liquid nitrogen (LN_2) and room temperature (RT), a distinct change in cross-sectional microstructure can be observed (FIGS. **2** panels b and c). In LN_2 SMAT, the elongated grains were found to be fragmented adjacent to the impact surface along with the plastic flow of grains due to the high strain rate of plastic deformation. In RT SMAT, a similar microstructural change was observed along with a significant plastic flow of grains to 100 μm from the impact surface. In both SMAT samples, the second phase particles along the grain boundaries were found to flow with deformed grains.

[0071] Microstructural change on the impacted surface and across the cross-section was characterized using SEM (FIG. **3**). FIG. **3** panel a shows a collage of SMAT surfaces of the LN_2 SMAT and RT SMAT conditions. The undeformed surface (FIG. **3** panel d) shows two types of second-phase particles. The first one is a bright phase mainly composed of Cu and Fe along with Al and is related to either Al_7Cu_2Fe or $Al_{23}Fe_4Cu$ intermetallic phase similar to earlier work[51]. Second, a darker color phase is mainly composed of Mg and Si, Mg_2Si inclusion phase[50]. However, deformed SMAT surfaces showed an evolution of a different second phase with no trace of $Al_7Cu_2Fe/Al_{23}Fe_4Cu$ and Mg_2Si on the surface (FIG. **3** panel b and 3 panel c). These phases are mostly composed of Cu and Si along with Al. Elemental compositions for the second phase were listed in Table 3 and FIG. **12**. The cross-sectional SEM micrographs of SMAT surfaces show an inhomogeneous layer of bright Al—Cu—Si phase with no trace of Al_7Cu_2Fe and Mg_2Si second phase near the impact surface (FIG. **3** panels e and f).

[0072] Table 3: EDS analysis (in at. %) of matrix and second phases in undeformed and SMAT samples with the location mentioned in FIG. **12**.

	Cu	Fe	Zn	Mg	Si	Al	Cr
1	41.26	—	—	—	17.51	41.23	—
2	31.16	—	—	—	10.22	58.62	—
3	03.47	12.66	—	—	—	83.36	00.50
4	—	—	01.33	13.03	26.51	59.13	—
5	12.56	05.67	—	01.90	—	79.87	—

[0073] To understand the variation in grain size and evolution of second phases close to the SMAT surface, scanning transmission electron microscopy (STEM) characterization was performed and the results are depicted in FIG. **4**. The LN_2 SMAT sample shows nanocrystalline grains close to the SMAT surface and the grain size gradually increases with an increase in distance from the surface (FIGS. **4** panel a and **4** panel b). In addition, Z (atomic number) contrast in the HAADF image indicates the presence of two bright second phase particles along the grain boundaries, and the grain boundaries were also found to be decorated by a higher Z element compared to the aluminum matrix (FIG. **4** panel a). In the case of RT SMAT, similar nanocrystalline grains can be observed, however, the gradient in grain size was not as prominent as in LN_2 SMAT (FIGS. **4** panel c and **4** panel d). This can be due to the higher depth of fragmented nanocrystalline grains in the RT SMAT as observed in FIG. **2**. Next, the second phase particles in RT SMAT were found to be smaller in size compared to LN_2 SMAT. The EDS line profile and EDS mapping (FIG. **4** panels f-h and FIG. **13**) illustrate that the bright phases are composed of either Si or Cu. The Cu-based phases are found to be higher in volume fraction than Si-based phases in both SMAT samples. Additionally, Si-based phases were found to be comparatively higher in volume fraction in the RT SMAT sample than in LN_2 SMAT. Besides, some of the bright second-phase particles were also found to be rich in Zn, but their volume fraction was found to be smaller than the Cu and Si-rich particles (FIG. **4** panel f and FIG. **4** panel h). Like the SEM images, the STEM image also indicates the dissolution of inherent Al—Cu—Fe and Mg_2Si phases. In addition, no trace of $MgZn_2$ (q) precipitates was observed in the STEM micrograph suggesting SMAT-induced dissolution. The average grain size of the top 500 nm layer from the impact surface was found to be 44 and 40 nm for LN_2 SMAT and RT SMAT, respectively (FIG. **4** panel e).

[0074] FIG. **5** shows the XRD patterns of the unimpacted base surface and the two SMAT surfaces (perpendicular to the rolling direction). In FIG. **5** panel a, the unimpacted surface shows a comparatively higher intensity for the (311) planes compared to the (220) planes indicating a presence of initial texture in the rolled plated sample. However, with

SMAT a sharp drop in (311) plane peak intensity can be observed which indicates a nearly random orientation has been achieved on the impacted surfaces. FIG. **5** panel b shows a broadening of full width at half maxima (FWHM) of the pure aluminum peaks along with a higher angle shift in peak position. The peak broadening can be assigned to the accumulation of micro-strain and grain refinement caused by SMAT. Next, in the SMAT samples, the peak positions were shifted towards a higher two-theta value indicating a combined effect of solute element saturation in the aluminum matrix and compressive residual stress. Further, between LN_2 and RT SMAT samples, the latter has a higher peak broadening and two-theta shift indicating higher micro-strain and residual stress. Lastly, FIG. **5** panel c shows the low-intensity peak for all three surfaces, where the base indicates the presence of Al—Fe—Cu and $MgZn_2$ phases. Whereas SMAT surfaces illustrate the presence of Al—Cu and Si and dissolution of $MgZn_2$ and Al—Cu—Fe phases. Hence, the SMAT process has not only created a gradient microstructure with the shear plastic flow of elongated grains but also dissolved the inherent second phases and formed ones. These microstructural changes can alter the electrochemical response to a large extent and will be characterized through electrochemical tests and discussed herein.

[0075] Electrochemical Characterization

[0076] The corrosion potential for a sample having equilibrium between anodic and cathodic kinetics (minimum current density) can be measured through an Open Circuit Potential (OCP)[51]. FIG. **6** panel a shows the OCP curves for the base, LN_2 SMAT, and RT SMAT samples. The OCP of the base increases to a more positive value with time and stabilizes close to 0.8 VSCE after 300 sec of immersion. However, SMAT samples showed a relatively stable OCP from the beginning of immersion compared to the base sample. The stabilized OCP value of the RT SMAT sample was found similar to the base, however, for the LN_2 SMAT sample, the stabilized OCP value is about 20 mV negative relative to the other two alloys. These changes in OCP behavior can be due to changes in the surface microstructure upon SMAT processing. In the case of the base, the increase in OCP (after immersion) before stabilization can be explained by dealloying and dissolution of Mg_2Si and $\eta(MgZn_2)$ precipitate[52]. However, in the case of SMAT samples dissolution of t and Mg_2Si phases and formation of Al—Cu-based phases have created a more stable OCP from the beginning of immersion[52]. Similar dissolution of the i phase due to surface severe plastic deformation has been observed[13,53]. Comparing the RT SMAT and LN_2 SMAT samples, the difference in stabilized OCP can be due to the difference in the volume fraction of precipitated second phase particles and the amount of residual stress on the surface.

[0077] The applied potential-driven surface phenomena can be analyzed through potentiodynamic polarization and cyclic potentiodynamic polarization for all three samples (FIGS. **6** panel b and **6** panel c). In FIG. **6** panel b, the base sample shows a rapid increase in anodic current density after OCP and followed by a second breakdown potential in the curve close to 0.75 VSCE. The sudden increase in current density after OCP is related to the dissolution of the altered surface layer generated by polishing and the second breakdown potential can be co-related to the initiation of localized pitting and intergranular corrosion (IGC) 4. In the case of the SMAT samples, the current density in both cathodic and anodic regimes was found to be decreased in comparison to the base sample. The LN_2 SMAT sample showed the smallest cathodic current density whereas the anodic current density for the RT SMAT sample was found to be the smallest among the three alloys. Unlike the base sample, both the SMAT processed alloys didn't show a second breakdown potential after OCP indicating the underlying microstructural change due to SMAT has altered both the oxide layer formation as well as the corrosion mechanism. The equilibrium potential (E_{corr}) values were found to be in agreement with the stabilized OCP values shown in FIG. **6** panel a. The corrosion current density (i_{corr}) for the SMAT alloy was smaller than the base alloy, indicating that SMAT has improved the overall corrosion resistance. In cyclic potentiodynamic polarization curves (FIG. **6** panel c) forward cycles for all alloys were similar to the polarization curves (FIG. **6** panel b) and the curve reversed after reaching a pre-defined reverse current density (i_{rev}) of 5 $mAcm^{-2}$. The potential (E_{sw}) at which the curve reached the i_{rev} was found to be most positive for the RT SMAT sample followed by the LN_2 SMAT and the base samples. However, in the reverse cycle, the protection potential (E_{prot}) is found to be most negative for the RT SMAT sample followed by the LN_2 SMAT and the base samples. It indicates that SMAT treated samples need higher overpotential (E_{corr}–E_{prot}) to repassivate compared to base (untreated alloy) and it seems counter-intuitive with potentiodynamic polarization results where SMAT sample showed better corrosion resistance. But it can be noted that the E_{sw} for the RT SMAT sample is most positive, hence for the roughly same amount of charge passed (as i_{rev}=5 $mAcm^{-2}$ and same scan rate) for all samples, the RT SMAT surface can create larger pits compared to the base which can have a large number of smaller pits. Hence, larger pits in SMAT can eventually lead to a higher driving force for repassivation. A similar opposite trend in polarization and cyclic polarization results have been observed[55], where it was observed that for an Al—Zn—Mg alloy lower overpotential was needed for repassivation in higher [Cl^-] solutions as compared to lower [Cl^-] solutions although the former have higher susceptibility of pitting corrosion. Apart from this, an increase in the surface micro-roughness due to SMAT can also hinder the repassivation behavior.

[0078] Electrochemical impedance spectroscopy (EIS) measurements were performed at different immersion times (0.5, 2, 6, 12, 24, 48 h) to investigate the time-dependent surface evolution. The measurements were plotted as Nyquist, Bode-bode, and Bode-phase angle plots for the three alloys (FIG. **7**). Nyquist plots at 0.5 hr for each sample were found to consist of two capacitive and an inductive loop at high, medium, and low-frequency domains. The high-frequency capacitive loop represents a double layer inhomogeneous oxide film (Al_2O_3) which consists of a porous thick hydrated oxide film at the oxide/solution interface and a thin continuous compact film at the metal/oxide interface[56,57]. Similarly, the medium to low-frequency capacitive loop represents double-layer capacitance at the film-solution interface and active metal dissolution pits[58]. This loop is more prominent in SMAT samples. With an increase in immersion time, the overall diameter of the Nyquist plot was found to decrease in each sample with a large depression in the second capacitive loop, which can be attributed to a weakening of a passive oxide layer with

exposure to aggressive Cl^- ion and the increase in metal dissolution from the oxide-free surface. Furthermore, the low-frequency inductive loop corresponds to the faradic reaction and the adsorption/desorption of charged species and their relaxation process at the interface[59-61]. Lastly, in the base alloy at 24 and 48 hr a semi-Warburg type impedance behavior can be seen that can correspond to diffusion-limited resistance provided by Al $(OH)_3$ corrosion product formed on the surface by the below-mentioned reactions (1)-(3) 62-64:

$$Al \rightarrow Al^{3+} + 3e^- \quad (1)$$

$$O^2 + H_2O + 4e^- \rightarrow 4OH^- \quad (2)$$

$$Al^3 + + 3OH^- \rightarrow Al(OH)_3 \quad (3)$$

[0079] The |Z| value for all the samples can be observed in FIG. **7** panels b, e, and h where with time, the |Z| value is found to decrease and saturate as immersion time increases. Similarly, the bode phase angle plot (FIG. **7** panels c, f, and i) show a clearer representation of transition in various components over the frequency range. In between 10 to 1000 Hz, one time constant can be observed in the bode plot representing the oxide layer contribution and at 0.1 to 0.01 Hz there is a second time constant that represents the contribution from double-layer capacitance.

[0080] Equivalent circuits displayed in FIG. **8** panel a were used to fit the measured impedance spectra. In the circuits R_s represents solution resistance, CPE_{ox} and CPE_{dl} indicate oxide layer capacitance and double-layer capacitance. Likewise, R_{ox} and R_t are resistances to ion transport in the oxide layer and charge transfer resistance on an active dissolving surface. Lastly, L, R_L, and W indicate inductance and resistance corresponding to the inductor and Warburg impedance at low-frequency domains. Parameters obtained through filling were listed in Table 4.

[0081] Table 4: Values of electrochemical parameters were obtained from filling the EIS curves with the equivalent circuits.

[0082] Variation of surface film resistance with immersion time for three samples was shown in FIG. **8** panel b. With the increase in immersion time, the resistance values gradually drop followed by stabilization at 12 hr and higher immersion time. The RT SMAT sample showed the highest resistance throughout the immersion time compared to the other two samples. Comparing the LN_2 SMAT and base samples, the former was found to have smaller resistance till reaching 6 hrs and again at 24 hrs and 48 hr of immersion, the trend flips. Variation of effective capacitance (C_{eff}) value for the surface film with immersion time was extracted from CPE_f presented in FIG. **8** panel c. The CPE_f represents a non-ideal capacitance contribution from the surface film as the phase angle is not exactly−90° (FIG. **7** panels c, f, and i). The value of C_{eff} for the surface film can be expressed by equation (4) (see Hsu and Mansfeld)[65,66].

$$C_{eff} = Q_f^{\frac{1}{\alpha}} R_f^{\frac{(1-\alpha)}{\alpha}} \quad (4)$$

[0083] Where R_f represents the surface film resistance, Q_f and α are the CPE_f parameters. The thickness of the surface film is inversely proportional to C_{eff} by equation (6)[67]:

$$C_{eff} = \frac{\varepsilon\varepsilon_0}{d_f} \quad (5)$$

[0084] Where d_f represents the thickness of the surface film, ε_0 is the permittivity of the vacuum and ε is the dielectric constant of the surface film. So, it can be inferred from FIG. **8** panel c that the base sample has a thicker film compared to SMAT samples, and among LN_2 SMAT and RT SMAT the latter has a relatively thicker film in all immersion times. Although the base has a thicker film, its lower film resistance makes it more susceptible to the corrosive environment[67].

TABLE 4

Values of electrochemical parameters were obtained from fitting the EIS curves with the equivalent circuits.

	Time (hrs.)	R⍰ (Ω · cm²)	Q⍰ (μF · cn⍰)	⍰	R⍰ (Ω · cm²)	Q⍰ (μF · cn⍰)	⍰	R⍰ (Ω · cm²)	L (H · cn⍰)	R⍰ (Ω · cm²)	W (Ω⍰)
Base	0.5	1.8	9.56	⍰	3243	71.7	0.67	1053	3508	1310	—
	2	1.7	19.1	0.91	2312	671	0.7	186.3	675.6	381.3	—
	6	1.4	28.7	0.93	1903	9060	1	79.86	25166	1463	—
	12	1.5	36.9	0.92	2016	2170	1	406.8	43862	3522	—
	24	1.4	46.3	0.91	1867	1300	0.93	1218	—	—	⍰
	48	1.3	61.9	0.89	1743	1060	0.95	1325	—	—	204.5
⍰	0.5	2.2	14.3	0.90	2586	337	1	⍰	⍰	1206	—
SMAT											
	2	2.3	36.7	0.89	2056	992	1	1113	25503	987.5	—
	6	2.3	57.3	0.89	1453	505	0.72	1464	35196	1283	—
	12	2.3	90.6	0.87	1898	1560	1	389	44268	1813	—
	24	2.4	114	0.87	1956	1830	1	269.4	29874	1905	—
	48	2.4	163	⍰	1951	2760	1	265.8	60980	4030	—
RT	0.5	2.5	9.68	0.86	5575	⍰	0.81	⍰	190290	4007	—
SMAT											
	2	2.7	21.6	0.90	4166	754	1	4331	119025	2027	—
	6	2.8	36.2	0.91	4536	703	1	5469	501215	4554	—
	12	1.5	45	0.92	3517	1060	1	740.5	57358	2128	—
	24	1.6	65.3	0.91	3651	4520	1	417	66382	6625	—
	48	1.6	94.7	0.90	3616	1750	1	1758	568719	1177	—

⍰ indicates text missing or illegible when filed

[0085] Intergranular Corrosion (IGC) Measurements

[0086] AA7xxx series alloys undergo intergranular corrosion (IGC) when exposed to a corrosive medium due to the anodic dissolution of grain boundary precipitate. To investigate the effect of SMAT on IGC susceptibility, ASTM G110-based immersion testing was performed for each sample. After immersion testing, optical micrographs were performed on the alloy cross-section as shown in FIG. **9** panels a-c. For the base alloy (FIG. **9** panel a), the grain boundaries parallel to the rolling direction were dissolved after 24 hours of immersion. Along with grain boundary, some grain dissolution can be observed in the enlarged micrograph shown in the insert of FIG. **9** panel a. Comparing the IGC profile of LN_2 SMAT and RT SMAT samples with the base sample (FIG. **9** panels b and c), it can be inferred that grain boundary dissolution has occurred along the plastically flowed elongated grains due to the high strain rate impact of aluminum-coated stainless-steel balls. Moreover, a severe dissolution of highly deformed grains near the impacted surface was observed in the enlarged micrograph shown in the inserts of FIG. **9** panels b and c. This can be due to the high reactivity of severely deformed nanocrystalline grains formed via SMAT processing. The IGC depths for all three alloys were measured from several similar optical micrographs and the percentage variation of IGC depth in three alloys was shown as a histogram plot in FIG. **9** panel d. It can be observed from the plot that the RT SMAT sample has maximum IGC penetration depths of around 50-75 μm, LN_2 SMAT alloy has around 100-125 μm and the base alloy varies from 75-150 μm. However, for the base alloy, a high fraction of IGC depth was observed above 200 μm than in SMAT samples. Without wishing to be bound by theory, the SMAT process, the sacrificial dissolution of high-energy nanograins close to the impact surface and the torturous path provided by shear flowed elongated grains have minimized the average IGC penetration depth in comparison to the base sample.

[0087] Secondary Ion Mass Spectroscopy and X-Ray Photo Spectroscopy Characterization

[0088] To understand the surface oxide layer modification through SMAT, time of flight-secondary ion mass spectroscopy (ToF-SIMS) characterization was performed on three alloy surfaces after 15 min of immersion in 0.6 M NaCl solution at open circuit potentials. FIG. **10** panels a-c shows the general ion depth profile as a function of Cs^+ ion sputtering time. The concentration profiles were plotted on a logarithmic scale to visualize low concentration change and the variation with time represents the in-depth ion concentration variation from the top alloy surface layer. In each alloy's depth profile, three regions can be identified. The first region has a quasi-constant AlO_2^- and O_{16}^- the concentration represents the aluminum oxide and the oxygen concentration represents the oxide layer. The O_{16}^- was used instead of O_{18}^- because of the latter causes saturation of the detector. The first region extends up to the time when the AlO_2^- and O_{16}^- reaches the maximum. In this region, a small and gradually increasing concentration for Al_2^- (represents metallic aluminum) for all three alloys. Cu^- which represents the copper concentration revealed different behavior in base and SMAT alloys. In SMAT alloys, Cu^- ion maxima were observed in the center of the oxide layer, unlike the base alloy, suggesting copper enrichment through selective oxidation of Al due to the Al—Cu-based second phase generated through SMAT. The Cu enrichment under the Al oxide film has been observed in studies on Al—Cu thin films[68,69]. The SiO_2, which represents the silicon dioxide concentration shows a sharp drop in the oxide region of base alloy; however, in SMAT alloys, the concentration is steady. The Cl^- and OH^- represents the contribution from corrosion product and aluminum hydroxide and their concentration reduces after reaching a maximum near the surface. SMAT samples showed a comparatively higher thickness (i.e., 423 and 463 seconds of sputtering time for LN_2 SMAT and RT SMAT, respectively) relative to the base sample (104 seconds of sputtering time). Following the oxide layer, the interface region begins till the innermost substrate starts. The interface region thickness depends on sample surface roughness and that is the reason the SMAT alloys show higher interface region thickness as compared to the base alloy. In this region Cu^- undergo a minimum in concentration for LN_2 SMAT and RT SMAT before increasing again till the substrate region where the concentration stabilizes. The AlO_2^- concentration was found to decrease in this region for the base alloy; however, for SMAT alloys the AlO_2 concentration is found relatively constant before it decreases from the beginning of the substrate region. In the substrate region a sharp increase in Al_2^-, stabilization of Cu^- and drop-in AlO_2^- and O_{16}^- was observed.

[0089] X-ray photoelectron spectroscopy (XPS) scans were performed on three alloys after 15 min of immersion in 0.6M NaCl solution (FIG. **10** panel d). The main components observed were aluminum, oxygen, and carbon. To capture the presence of these elements Al 2p, 0 Is, and C Is, high-resolution spectrums were obtained (FIG. **10** panels e-g). In addition, the presence of minor elements such as zinc and silicon were obtained through Zn 2p, and Si 2p high-resolution spectra (FIG. **10** panels h and i). The C Is high-resolution used as a calibration reference spectrum has four components: at 284.6 eV (C—C), 286.1 eV (C—O), 287.2 eV (C—O═C) and 289 eV (presence of CO_3^{2-}) bonds, respectively (FIG. **10** panel e). The presence of carbon comes from the surroundings as contamination[70]. Additionally, the C 1s, and O 1s peaks were deconvoluted into three components: 530.53 eV (O_2—), 531.83 eV (presence of OH components), and 532.73 eV (presence of water and C═O bonds) (FIG. **10** panel f)[1]. In the case of Aluminum, as shown in FIG. **10** panel g, Al 2p was designated as the Al^{3+} component, which indicates the presence of aluminum oxide and hydroxide (FIG. **10** panel g)[72]. The chemical composition of the surface film has been tabulated in Table 1. It can be observed that the surface layer is mainly composed of O, C, and Al from which Al is found to be mostly present as aluminum hydroxide and C as contamination from the environment. In addition, the RT SMAT sample shows the absence of a Zn peak indicating the dissolution of η precipitates (FIG. **10** panel h). Surprisingly there was no indication of Cu as a component on the surface layer (Table 1), which can be due to the presence of copper in the inner layer of the film and was observed during sputtering in TOF-SIMS characterization (FIGS. **10** panels b and c). Lastly, in SMAT samples, RT SMAT (FIG. **10** panel i) sample shows a comparatively higher fraction of the Si component which can be attributed to a higher fraction of the Si phase compared to LN_2 SMAT.

TABLE 1

XPS data of three alloys showing the calculated chemical composition of the surface film (in at %).

Elements	Base	LN_2 SMAT	RT SMAT
Al 2p	21.4	16.12	5.21
O^{2-}	7.2	5.6	1.9
OH—	24.9	26.3	11.5
CO_3^{2-}/H_2O	14.4	3.1	6.7
C 1s	30.92	48.42	74.26
Zn 2p	0.34	0.3	0
Si 2p	0.77	0.16	0.41

[0090] Quasi In-Situ Post Corrosion Surface Characterization

[0091] To understand the onset of localized corrosion and its propagation with time, sample surfaces were characterized after immersion in 0.6 M NaCl solution for 6 hr and 24 hr. Towards this, the same region was tracked for each sample after different immersion times and the results are presented in FIG. **11**. Note that the micrographs in FIG. **11** for each sample are magnified images from FIG. **14**. As prepared base sample (FIG. **11** panel a) shows the presence of bright Al_7Cu_2Fe and dark Mg_2Si intermetallic phase. After 6 hr of immersion, the localized dissolution of the aluminum matrix adjacent to the Al_7Fe_2Cu phase was evident, which is highlighted using red arrows as shown in FIG. **11** panel b. In addition, dissolution of matrix around nanoscale precipitates decorated along grain boundaries was also observed (shown in green arrows). Furthermore, the Mg_2Si phase undergoes selective dissolution of Mg[73], leaving behind Si which further undergoes passivation to form SiO_2 as detected in SIMS ion depth profile (FIG. **10** panel a)[74]. In contrast, in SMAT specimens, processing-induced surface roughness can be observed with the distribution of sub-micron to few microns range Al—Cu based phases, shown by red arrows in FIG. **11** panels d and g. After 6 hr of immersion, the localized dissolution around these cathodic phases was observed in SMAT conditions (FIG. **11** panels e & h). After 24 hr of immersion, the deposition of white corrosion products was found around the matrix and over the second phase particles. Deposition of corrosion product with time provides a hindrance effect towards transport of ionic species towards and away from the corroding sites (FIG. **11** panels c, f, & i). Moreover, in the base sample, the intergranular and intragranular matrix dissolution and dealloying of Al_7Cu_2Fe was observed (FIG. **11** panel c).

DISCUSSION

[0092] The results showed that SMAT processing in different environments introduced a large amount of plastic deformation into the base aluminum 7075 alloy surface, which significantly altered the surface microstructure and improved the corrosion resistance of the aluminum alloy. In both of the SMAT samples, an ultra-fine layer of grains was present close to the impact surface and followed by a region of shear flowed elongated grain. In addition to grain size refinement, dissolution of inherent second phases ($Al_7Cu_2Fe/Al_{23}Fe_4Cu$ and Mg_2Si), and precipitation of Al—Cu, Si, and Zn phases were observed near the impact surface. The SMAT-treated samples exhibited increased corrosion resistance due to the combined beneficial effect of grain size refinement, absorption, and second-phase precipitation. In the subsections herein, microstructure evolution and the observed improvement in corrosion resistance will be discussed separately.

[0093] Precipitation of Al—Cu Based Phases in Ultrafine Layer

[0094] The η ($MgZn_2$) phase is the primary hardening precipitate found in Al—Zn—Cu—Mg-based alloys. This strengthening phase is distributed within the matrix and along the grain boundaries[75]. In embodiments, the base alloy was in peak-age (T6) condition, hence the aluminum matrix will have η' incoherent precipitate and the presence of $MgZn_2$ was confirmed using XRD (FIG. **5** panel c). However, in the SMAT processed samples, the absence of the relevant XRD peaks and the absence of observation from TEM analysis indicated that SMAT processing has affectively dissolved/solutionized η' precipitates back into the matrix. Similar, fragmentation and dissolution of precipitates through SPD processing have been observed in Al-1.7 at. % Cu alloy[76], 7055-T77[53], and 7034[77] alloys. In addition to the dissolution of 11' precipitates, the surface close to the impact surface was also found to be deprived of Al_7Cu_2Fe and Mg_2Si intermetallic phases (FIG. **3**). This indicates that the high strain rate impact of aluminum-coated steel balls has also fragmented and dissolved these phases near the impact surface. Hence, the dissolution of multiple phases can have created a supersaturated solid solution of Zn, Mg, Cu, Si, and Fe in the aluminum matrix.

[0095] Precipitation of AlCu, $Al_2Cu(\theta)$, Si, and Zn from the supersaturated solid solution is interesting. Similar phenomena have been observed in the altered surface layer (ASL) of AA7055 alloy after surface abrasion[53]. In the same study, Wang et al. suggested the following mechanism for the precipitation of AlCu and θ phases. The supersaturated solid solution in ASL after the dissolution of η and η' precipitates was shown to drive the nucleation of AlCu, θ, and Zn phases through vacancy, dislocations, and grain boundaries assisted diffusion of solute atoms. These precipitates later coarsened at 200 nm in length after natural aging for 42 months. In contrast, in this work, θ precipitates of 2-4 μm in diameter were observed after 30 minutes of SMAT processing (FIG. **3**). In embodiments, the precipitate can enhance corrosion protection. In addition, precipitation of pure Si (FIG. **4** panels a and c) was observed in both RT SMAT and LN_2 SMAT samples, which has not been observed in the aluminum 7075 alloy reported earlier. This indicates that heavy plastic deformation through the continuous impact of high-velocity aluminum-coated stainless-steel balls has not only increased the amount of non-equilibrium defects but also increased the localized surface temperature, which has enhanced the kinetics of precipitation significantly. The preferential formation of pure Si, Al—Cu-based, and Zn phases can be described by the interaction tendency of solute atoms towards the vacancies. The vacancy binding tendency of each solute atom can be arranged in following order Si (0.08 eV)>Zn (0.03 eV)>Cu (0.02 eV)>Fe (−0.00)>Mg (−0.02)[78]. Being most favorable Si and Zn were found to form pure elemental phases. Vacancy-mediated diffusion helps to transport solute atoms from the grain interior to the nearby dislocations and grain boundaries.

[0096] Improvement is Corrosion Resistance Through SMAT Processing

[0097] Collectively, polarization and EIS measurement indicate that with SMAT processing, specifically in RT

SMAT there is a reduction in anodic and cathodic current density and an increase in film resistance. In the aluminum alloy, the underlying interfacial mechanism for corrosion can be summarized into a series of steps, i.e., adsorption of Cl^- ion onto the oxide layer[79], the interaction of Cl^- with oxide layer[80,81], exposure of substrate and formation of metastable pits, and finally metastable pit converting to stable pit depending on pit environment[82]. The relationship between the surface microstructure of each specimen with the interfacial mechanism was carried out to investigate the improved corrosion resistance with SMAT.

[0098] In the base specimen, the surface microstructure consists of second phases such as Al_7Cu_2Fe, Mg_2Si, and $MgZn_2$ along with solute elements in the matrix. This microstructure dictates the alloy's pitting and intergranular corrosion susceptibility[54,83,84]. The polarization curve of the base sample showed two breakdown potentials similar to earlier work by Wang et al.[83]. The two-breakdown potentials are due to the difference in solute content, specifically (Cu and Zn) between the ASL and the underlying matrix. In EIS measurement, after 0.5 hr of immersion presence of an inductive loop and the absence of a second capacitive loop indicates the localized breakdown of an oxide film and initiation of anodic dissolution (FIG. **7** panel a). With further progress in corrosion, the overall diameter of a capacitive loop in the Nyquist plot was found to decrease and the pitting corrosion in this specimen can be observed from post 6 hr of immersion microstructure (FIG. **11** panel b). Additionally, the dissolved Al^{3+} ions can interact with OH^- ions to precipitate Al $(OH)_3$ product layer, which was indicated through the SIMS depth profile (FIG. **10** panel a), XPS surface spectrum (FIG. **10** panel f), and post corrosion surface characterization (FIG. **11** panel c). At higher immersion times, the higher volume of these corrosion products (FIG. **11** panel c) can provide resistance to the mass transport of ions and its response can be visualized by Warburg impedance in the Nyquist plot (FIG. **7** panel a).

[0099] In the case of RT SMAT surface grain size refinement, precipitation of pure Si and Al—Cu-based phases and dissolution of inherent phases were observed. The average grain size of SMAT samples close to the impact surface is ~30 nm which can enhance the reactivity of oxygen with surface elements by providing nucleation spots and diffusion pathways for elemental and ionic species. It can be correlated to a higher thickness of the oxide layer in the SMAT samples compared to the base sample observed through the ToF-SIMS ion depth profile (FIG. **10** panels a-c). Similarly, through equal channel angular pressing (ECAP), Ralston et al.[12] have achieved an average grain size (refinement) of 125 μm in pure aluminum, which was shown to improve the surface reactivity and ion diffusion through higher grain boundary density. Furthermore, oxidation of pure Si phases in SMAT sample has shown to form SiO_2 in the oxide layer and found to be more stable in concentration in RT SMAT sample through ToF-SIMS sputtering (FIG. **10** panel c). SiO_2 with lower pH of zero charges (pH_{pzc}~2.0)[85] can reduce the overall pH_{pzc} of Al_2O_3(−9.5)[85] and can slow down the adsorption of Cl^- ion on the oxide surface. A thicker and compound oxide layer in RT SMAT sample can contribute to the observed reduction in anodic kinetics and higher CPE_1 and CPE_2 value in the Nyquist plot for 0.5 hr. Next, considering the effect of the dissolution of inherent second phases and the formation of different phases, their size, distribution, and galvanic coupling propensity can affect the cathodic activity of these phases[86-88]. In the base alloy, considering the corrosion potential w.r.t. standard calomel electrode (SCE), Al_7Cu_2Fe (−654 mV_{SCE}) will act as a cathode, whereas Mg_2Si (−1536 mV_{SCE}) and $MgZn_2$ (−1095 mV_{SCE}) will act as an anode for 7075 aluminum matrix (~−800 mV_{SCE})[87]. Similarly, in the case of SMAT alloys, Al—Cu phases (−695 mV_{SCE}) and Si (−452 mV_{SCE}) will act as cathode and Zn (−1098 mV_{SCE}) as anode for the aluminum matrix[87]. It can be noted that after SMAT, Fe and Mg were mostly found retained within the matrix as a solid solution due to a lower vacancy binding tendency as compared to other elements. Among Al_7Cu_2Fe and Al—Cu phase, later will act as a weaker cathode towards the matrix. However, Si which is a stronger cathode compared to Al_7Cu_2Fe and Al—Cu will stay inert in a near-neutral solution and can form amorphous SiO_2 as indicated by Kairy et al[74]. The presence of SiO_2 in the SMAT sample was indicated through the ToF-SIMS ion depth profile (FIG. **10** panels b and c). Furthermore, the size of second phases on SMAT surface were found to be in nanometer range which will reduce their cathodic activity by the 'small cathode and large anode' mechanism[86,89]. For instance, Osorio et al. have found that fine and homogenous Al_2Cu (θ) phases with fine dendritic spacing can provide galvanic protection to the aluminum matrix[90]. Hence the dissolution of Al_7Cu_2Fe phases with precipitation of small Al—Cu-based phases can be attributed to a reduction in cathodic kinetics in SMAT samples.

[0100] In conclusion, surface mechanical attrition treatment (SMAT) of Al 7075-T6 with aluminum-coated steel balls was performed at room and LN_2 temperatures to obtain a gradient nanostructure surface layer. The listed points are non-limiting findings described herein:

[0101] Microstructural characterization and XRD analysis of the SMAT surfaces revealed a nano-grained surface layer with precipitation of AlCu, Al_2Cu (θ), Si, and Zn phases. In addition, dissolution of inherent phases, i.e., Al_7Cu_2Fe, Mg_2Si, and $MgZn_2$ close to SMAT surface was observed.

[0102] Potentiodynamic polarization showed a reduction in the anodic and cathodic kinetics in SMAT processed samples relative to the base sample. Among the three conditions, the RT SMAT exhibited the lowest anodic dissolution rate.

[0103] EIS measurements for two days of immersion revealed that the RT SMAT has the highest polarization resistance among all samples tested under all immersion times. In addition, the SMAT processed sample showed a comparatively stable surface film in lower immersion times relative to the base alloy.

[0104] Surface film characterization through the TOF-SIMS revealed a thicker oxide film with Cu and SiO_2 enrichment in SMAT processed samples due to the presence of Al—Cu phases and oxidation of Si.

Overall, the understanding gained through this work indicates a route to further improvement of corrosion-resistant of aluminum alloys and the design of corrosion-resistant light alloys for structural applications in the automotive and aerospace sector.

[0105] Methods

[0106] Materials

[0107] Described herein, an aluminum rolled plate from a Midwest steel and aluminum company was used with a T651 temper condition. Samples were sectioned into circular disks

from the rolled plate with a thickness of 6 mm and a diameter of 50 mm. The thickness of the disk was parallel to the rolling direction (RD). The composition of the as-received sample is provided in Table 2. Samples were polished till 1200 grit SiC paper followed by cleaning in an ultrasonication bath for 5 min and air-dried before surface mechanical attrition treatment (SMAT).

TABLE 2

Chemical composition of AA 7075-T651 (wt %/at %)

Al	Zn	Mg	Cu	Cr	Fe	Si	Mn	Ti
90.44/ 94.19	5.61/ 2.41	2.23/ 2.56	1.26/ 0.56	0.21/ 0.11	0.15/ 0.07	0.03/ 0.02	0.02/ 0.008	0.07/ 0.04

[0108] Surface Mechanical Attrition Treatment (SMAT)

[0109] SMAT was carried out using a SPEX 8000M high-energy ball milling machine. The prepared samples were used as an outer lid for the SPEX stainless steel vial along with 50 g of 6.35 mm diameter 440C stainless steel balls. A high-purity argon glove box was used to open and close the vial for each treatment. SMAT was performed at room temperature (RT SMAT) and inside a liquid nitrogen-flowing chamber (LN_2 SMAT) for 30 minutes. A SMAT duration of 30 minutes was chosen following earlier reported works[39]. To avoid contamination of iron from the surface of the milling media and the inner wall of the vial, these surfaces were coated with a layer of pure aluminum powder. This coating was achieved through cryogenic milling of 0.5 grams of pure aluminum powder, 325 mesh size (Alfa Aesar) for 1 hour with 5 minutes of the interval after every 15 minutes of milling. Resting in between the runs was used to avoid an increase in temperature that can lead to the agglomeration of aluminum particles. RT SMAT was performed by loading the vial into the SPEX 8000M mill, whereas for LN_2 SMAT the vial was inserted into a Teflon sleeve with the inflow and outflow of liquid nitrogen from the dewar.

[0110] Microstructural Characterization

[0111] Optical microscopy was used to visualize the effect of SMAT on cross-sectional surface grain structure. Disks were sectioned perpendicular to the SMAT surface and polished to a 0.05 μm diamond finish. Keller's reagent (95 ml H_2O, 2.5 ml HNO_3, 1.5 ml HCl, 1 ml HF) was used to etch the polished surface. FEI-XL30 Scanning electron microscopy (SEM) equipped with energy dispersive spectroscopy (EDS) was used to characterize the microstructural changes with SMAT through the characterization of the SMAT surface and the plane perpendicular to it. Samples for TEM characterization were lifted out from the SMAT surface using a Focused Ion beam (FIB) Helios 5 UX and eventually thinned to electron transparency. STEM images were captured at various magnifications using the aberration-corrected ARM 200F (JEOL) to assess the microstructure, such as grain size and second phases, close to the SMAT surface of RT and LN_2 SMAT specimen. More than 200 grains were sampled to generate an average grain size for each condition using ImageJ software. X-ray diffraction (XRD) measurements were performed using Aeris Panalytical X-ray Diffractometer.

[0112] Electrochemical Characterization

[0113] A Gamry 600 Potentiostat connected to a standard three-electrode cell was used to perform each electrochemical experiment. SMAT and base sample surfaces with an immersed area of 1 cm^2 were used as the working electrode. Platinum wire and standard calomel electrode (SCE) were used as counter and reference electrodes respectively. Electrochemical measurements were performed at ambient temperature (i.e. ~ 23±2° C.) in a naturally aerated 0.6 M NaCl solution with an initial pH of 6.5±0.2. The desired pH was obtained by adding dilute HCl and NaOH solutions. Potentiodynamic polarization (PP) measurements were measured after 10 min of immersion in open circuit potential (OCP). PP measurements were performed from −100 mV (vs OCP) to −700 mV_{SCE} potential with a scan rate of 0.167 $mVsec^{-1}$. Cyclic polarization measurements were performed after 10 min of OCP and all the scans were started at −50 mV (vs OCP) and reversed after it reached 5 $mAcm^{-2}$ current density. Scans were stopped once it reaches the cathodic branch in the reverse cycle. Similarly, Electrochemical impendence spectroscopy (EIS) measurements were performed after immersion in OCP conditions for different duration i.e. 0.5, 2, 6, 12, 24, and 48 hours. Measurements were performed with a sinusoidal voltage of 10 mV over a frequency range of 100 kHz to 10 MHz. Tafel plots and EIS plots were analyzed by EC-Lab software. Intergranular Corrosion (IGC) tests were performed according to ASTM G110[91], with a slight modification for health and safety precautions. Samples were pre-treated in 50 ml nitric acid (HNO_3)+950 ml deionized water for 1 min at 93° C. followed by 1 min in concentrated HNO_3 at room temperature. Samples were then cleaned with deionized water and dried with compressed air. The samples were then immersed in a solution of 57g NaCl+10 ml of H_2O_2+990 ml of deionized water for 24 hours. After immersion samples were thoroughly cleaned and sectioned and the cross-sections were polished and etched to reveal the microstructure. The propensity of IGC for each sample was calculated for the IGC depth from 30-50 fissures using ImageJ software. Quasi in-situ surface characterization was performed by analyzing the same region of the three samples after performing immersion in unbuffered 0.6 M NaCl solution with initial pH of 6.5±0.2 for 6 hr and 24 hr.

[0114] Secondary Ion Mass Spectrometry and X-Ray Photoelectron Spectroscopy Characterization

[0115] Time of flight-secondary ion mass spectrometer (ToF-SIMS) spectrometer (Ion-ToF IV GmbH, Monster, Germany) was used and all the measurements were performed under ultra-high vacuum conditions (10^{-9} mbar). 25 keV Ga+ ion was used as the primary source and 1 keV Cs^+ was used for sputtering. 100*100 μm^2 was analyzed from a sputtering area of 350*350 μm^2. The negative polarity ions were chosen for analyzing the surface. X-ray Photoelectron spectroscopy measurements were performed using Kratos Axis 165 Ultra X-ray Photoelectron Spectrometer. Monochromatic AlKα (1486.6 eV) was used and all the runs were carried out in 10^{-9} torr vacuum conditions. The analyzer pass energy was 100 eV for survey spectra and 20 eV for high-resolution spectra. The step size for wide spectrum was 1 eV and 0.1 eV for high resolution spectra. The photoelectron take-off angle (the angle of the surface with the direction in which the photoelectrons are analyzed) was 900 and a 400 μm spot size was used for each of the scans. Data processing (peak fitting and decomposition) was performed with the Casaxps software using iterative Shirley-type background subtraction and Gaussian/Lorentzian peak shapes.

REFERENCES CITED IN THIS EXAMPLE

[0116] 1. Lu, K. Making strong nanomaterials ductile with gradients. *Science* 345, 1455-1456 (2014).

[0117] 2. Fang, T. H., Li, W. L., Tao, N. R. & Lu, K. Revealing Extraordinary Intrinsic Tensile Plasticity in Gradient Nano-Grained Copper. *Science* 331, 1587-1590 (2011).

[0118] 3. Wu, X., Jiang, P., Chen, L., Yuan, F. & Zhu, Y. T. Extraordinary strain hardening by gradient structure. *Proc. Natl. Acad. Sci.* 111, 7197-7201 (2014).

[0119] 4. Lu, K. Stabilizing nanostructures in metals using grain and twin boundary architectures. *Nat. Rev. Mater.* 1, 16019 (2016).

[0120] 5. Wu, X. L. et al. Synergetic Strengthening by Gradient Structure. *Mater. Res. Lett.* 2, 185-191 (2014).

[0121] 6. Estrin, Y. et al. Architecturing materials at mesoscale: some current trends. *Mater. Res. Lett.* 9, 399-421 (2021).

[0122] 7. Tong, W. P. Nitriding Iron at Lower Temperatures. *Science* 299, 686-688 (2003).

[0123] 8. Balusamy, T., Kumar, S. & Sankara Narayanan, T. S. N. Effect of surface nanocrystallization on the corrosion behaviour of AISI 409 stainless steel. *Corros. Sci.* 52, 3826-3834 (2010).

[0124] 9. Roland, T., Retraint, D., Lu, K. & Lu, J. Fatigue life improvement through surface nanostructuring of stainless steel by means of surface mechanical attrition treatment. *Scr. Mater.* 54, 1949-1954 (2006).

[0125] 10. Chen, G. et al. Effect of surface mechanical attrition treatment on corrosion fatigue behavior of AZ31B magnesium alloy. *Int. J Fatigue* 127, 461-469 (2019).

[0126] 11. op't Hoog, C., Birbilis, N. & Estrin, Y. Corrosion of Pure Mg as a Function of Grain Size and Processing Route. *Adv. Eng. Mater.* 10, 579-582 (2008).

[0127] 12. Ralston, K. D., Fabijanic, D. & Birbilis, N. Effect of grain size on corrosion of high purity aluminium. *Electrochimica Acta* 56, 1729-1736 (2011).

[0128] 13. Pandey, V., Singh, J. K., Chattopadhyay, K., Srinivas, N. C. S. & Singh, V. Influence of ultrasonic shot peening on corrosion behavior of 7075 aluminum alloy. *J. Alloys Compd.* 723, 826-840 (2017).

[0129] 14. Jiang, X. P. et al. Enhancement of fatigue and corrosion properties of pure Ti by sandblasting. *Mater. Sci. Eng. A* 429, 30-35 (2006).

[0130] 15. Ren, X. D. et al. Microstructure evolution and grain refinement of Ti-6A1-4V alloy by laser shock processing. *Appl. Surf Sci.* 363, 44-49 (2016).

[0131] 16. Chui, P., Sun, K., Sun, C., Yang, X. & Shan, T. Effect of surface nanocrystallization induced by fast multiple rotation rolling on hardness and corrosion behavior of 316L stainless steel. *Appl. Surf Sci.* 257, 6787-6791 (2011).

[0132] 17. Masiha, H. R. et al. Effect of surface nanostructuring of aluminum alloy on post plasma electrolytic oxidation. *Appl. Surf Sci.* 317, 962-969 (2014).

[0133] 18. Chang, H.-W., Kelly, P. M., Shi, Y.-N. & Zhang, M.-X. Thermal stability of nanocrystallized surface produced by surface mechanical attrition treatment in aluminum alloys. *Surf Coat. Technol.* 206, 3970-3980 (2012).

[0134] 19. Darling, K. A., Tschopp, M. A., Roberts, A. J., Ligda, J. P. & Kecskes, L. J. Enhancing grain refinement in polycrystalline materials using surface mechanical attrition treatment at cryogenic temperatures. *Scr. Mater.* 69, 461-464 (2013).

[0135] 20. Shen, Y. et al. Ultrahigh Strength Copper Obtained by Surface Mechanical Attrition Treatment at Cryogenic Temperature. *J Mater. Eng. Perform.* 24, 5058-5064 (2015).

[0136] 21. Murdoch, H. A., Darling, K. A., Roberts, A. J. & Kecskes, L. Mechanical Behavior of Ultrafine Gradient Grain Structures Produced via Ambient and Cryogenic Surface Mechanical Attrition Treatment in Iron. *Metals* 5, 976-985 (2015).

[0137] 22. Novelli, M., Fundenberger, J.-J., Bocher, P. & Grosdidier, T. On the effectiveness of surface severe plastic deformation by shot peening at cryogenic temperature. *Appl. Surf Sci.* 389, 1169-1174 (2016).

[0138] 23. Liu, Y., Jin, B. & Lu, J. Mechanical properties and thermal stability of nanocrystallized pure aluminum produced by surface mechanical attrition treatment. *Mater. Sci. Eng. A* 636, 446-451 (2015).

[0139] 24. Rangaraju, N., Raghuram, T., Krishna, B. V., Rao, K. P. & Venugopal, P. Effect of cryo-rolling and annealing on microstructure and properties of commercially pure aluminium. *Mater. Sci. Eng. A* 398, 246-251 (2005).

[0140] 25. Pachla, W. et al. Mechanical properties and microstructure of ultrafine grained commercial purity aluminium prepared by cryo-hydrostatic extrusion. *Mater. Sci. Eng. A* 695, 178-192 (2017).

[0141] 26. Li, W. L., Tao, N. R. & Lu, K. Fabrication of a gradient nano-micro-structured surface layer on bulk copper by means of a surface mechanical grinding treatment. *Scr. Mater.* 59, 546-549 (2008).

[0142] 27. Zhang, J. et al. Bulk monolithic electrodes enabled by surface mechanical attrition treatment-facilitated dealloying. *J Mater. Chem. A* 4, 15057-15063 (2016).

[0143] 28. Zhao, J., Xia, W., Li, N. & Li, F. A gradient nano/micro-structured surface layer on copper induced by severe plasticity roller burnishing. *Trans. Nonferrous Met. Soc. China* 24, 441-448 (2014).

[0144] 29. Pu, Z. et al. Grain refined and basal textured surface produced by burnishing for improved corrosion performance of AZ31B Mg alloy. *Corros. Sci.* 57, 192-201 (2012).

[0145] 30. Technology Overview—MELD Manufacturing. https://meldmanufacturing.com/technology-overview/.

[0146] 31. Sun, Q., Han, Q., Xu, R., Zhao, K. & Li, J. Localized corrosion behaviour of AA7150 after ultrasonic shot peening: Corrosion depth vs. impact energy. *Corros. Sci.* 130, 218-230 (2018).

[0147] 32. Sun, Q. et al. A comparison of AA2024 and AA7150 subjected to ultrasonic shot peening: Microstructure, surface segregation and corrosion. *Surf Coat. Technol.* 337, 552-560 (2018).

[0148] 33. Wen, L., Wang, Y., Jin, Y. & Ren, X. Comparison of corrosion behaviour of nanocrystalline 2024-T4 Al alloy processed by surface mechanical attrition treatment with two different mediums. *Corros. Eng. Sci. Technol.* 50, 425-432 (2015).

[0149] 34. Wen, L., Wang, Y., Zhou, Y., Guo, L. & Ouyang, J.-H. Microstructure and corrosion resistance of modified 2024 Al alloy using surface mechanical attrition

treatment combined with microarc oxidation process. *Corros. Sci.* 53, 473-480 (2011).

[0150] 35. Fabijanic, D., Taylor, A., Ralston, K. D., Zhang, M.-X. & Birbilis, N. Influence of Surface Mechanical Attrition Treatment Attrition Media on the Surface Contamination and Corrosion of Magnesium. *CORROSION* 69, 527-535 (2013).

[0151] 36. Wen, M., Wen, C., Hodgson, P. & Li, Y. Thermal oxidation behaviour of bulk titanium with nanocrystalline surface layer. *Corros. Sci.* 59, 352-359 (2012).

[0152] 37. Benafia, S., Retraint, D., Yapi Brou, S., Panicaud, B. & Grosseau Poussard, J. L. Influence of Surface Mechanical Attrition Treatment on the oxidation behaviour of 316L stainless steel. *Corros. Sci.* 136, 188-200 (2018).

[0153] 38. Balusamy, T., Sankara Narayanan, T. S. N., Ravichandran, K., Park, I. S. & Lee, M. H. Influence of surface mechanical attrition treatment (SMAT) on the corrosion behaviour of AISI 304 stainless steel. *Corros. Sci.* 74, 332-344 (2013).

[0154] 39. Sun, Q., Han, Q., Liu, X., Xu, W. & Li, J. The effect of surface contamination on corrosion performance of ultrasonic shot peened 7150 Al alloy. *Surf Coat. Technol.* 328, 469-479 (2017).

[0155] 40. Li, N. et al. Effect of surface mechanical attrition treatment on biodegradable Mg-1Ca alloy. *Mater. Sci. Eng. C* 35, 314-321 (2014).

[0156] 41. Li, N. & Wang, N. The effect of duplex Surface mechanical attrition and nitriding treatment on corrosion resistance of stainless steel 316L. *Sci. Rep.* 8, 8454-8460 (2018).

[0157] 42. Olugbade, T. & Lu, J. Characterization of the Corrosion of Nanostructured 17-4 PH Stainless Steel by Surface Mechanical Attrition Treatment (SMAT). *Anal. Lett.* 52, 2454-2471 (2019).

[0158] 43. Fu, T. et al. Effect of surface mechanical attrition treatment on corrosion resistance of commercial pure titanium. *Surf Coat. Technol.* 280, 129-135 (2015).

[0159] 44. Du, H. et al. One way of surface alloying treatment on iron surface based on surface mechanical attrition treatment and heat treatment. *Appl. Surf Sci.* 255, 8660-8666 (2009).

[0160] 45. Sun, H. Q., Shi, Y. N., Zhang, M.-X. & Lu, K. Surface alloying of an Mg alloy subjected to surface mechanical attrition treatment. *Surf Coat. Technol.* 202, 3947-3953 (2008).

[0161] 46. Pouriamanesh, R., Vahdati-Khaki, J. & Mohammadi, Q. Coating of Al substrate by metallic Ni through mechanical alloying. *J Alloys Compd.* 488, 430-436 (2009).

[0162] 47. Revesz, A. & Takacs, L. Coating metals by surface mechanical attrition treatment. *J Alloys Compd.* 441, 111-114 (2007).

[0163] 48. Canakci, A., Erdemir, F., Varol, T. & Ozkaya, S. Formation of Fe—Al intermetallic coating on low-carbon steel by a novel mechanical alloying technique. *Powder Technol.* 247, 24-29 (2013).

[0164] 49. Romankov, S. et al. Effect of process parameters on the formation of Ti—Al coatings fabricated by mechanical milling. *J. Alloys Compd.* 484, 665-673 (2009).

[0165] 50. Singh, S. S. et al. 3D microstructural characterization and mechanical properties of constituent particles in Al 7075 alloys using X-ray synchrotron tomography and nanoindentation. *J Alloys Compd.* 602, 163-174 (2014).

[0166] 51. Davis, J. R. *Corrosion: understanding the basics*. (ASM International, 2000).

[0167] 52. Cavanaugh, M. K., Li, J.-C., Birbilis, N. & Buchheit, R. G. Electrochemical Characterization of Intermetallic Phases Common to Aluminum Alloys as a Function of Solution Temperature. *J Electrochem. Soc.* 161, C535-C543 (2014).

[0168] 53. Wang, S.-S. et al. Accelerated precipitation and growth of phases in an Al—Zn—Mg—Cu alloy processed by surface abrasion. *Acta Mater.* 131, 233-245 (2017).

[0169] 54. Meng, Q. & Frankel, G. S. Effect of Cu Content on Corrosion Behavior of 7xxx Series Aluminum Alloys. *J. Electrochem. Soc.* 151, B271 (2004).

[0170] 55. Zhou, S. et al. Effect of the chloride on passivity breakdown of Al—Zn—Mg alloy. *Corros. Sci.* 163, 108254 (2020).

[0171] 56. de Wit, J. H. W. & Lenderink, H. J. W. Electrochemical impedance spectroscopy as a tool to obtain mechanistic information on the passive behaviour of aluminium. *Electrochimica Acta* 41, 1111-1119 (1996).

[0172] 57. Hitzig, J., Juttner, K., Lorenz, W. J. & Paatsch, W. AC-Impedance Measurements on Corroded Porous Aluminum Oxide Films. *J Electrochem. Soc.* 133, 887-892 (1986).

[0173] 58. Hitzig, J., Juttner, K., Lorenz, W. J. & Paatsch, W. AC-impedance measurements on porous aluminium oxide films. *Corros. Sci.* 24, 945-952 (1984).

[0174] 59. Krawiec, H., Vignal, V., Amar, H. & Peyre, P. Local electrochemical impedance spectroscopy study of the influence of ageing in air and laser shock processing on the micro-electrochemical behaviour of AA2050-T8 aluminium alloy. *Electrochimica Acta* 56, 9581-9587 (2011).

[0175] 60. Huang, Y., Shih, H., Daugherty, J. & Mansfeld, F. Evaluation of the properties of anodized aluminum 6061 subjected to thermal cycling treatment using electrochemical impedance spectroscopy (EIS). *Corros. Sci.* 51, 2493-2501 (2009).

[0176] 61. Keddam, M., Kuntz, C., Takenouti, H., Schustert, D. & Zuili, D. Exfoliation corrosion of aluminium alloys examined by electrode impedance. *Electrochimica Acta* 42, 87-97 (1997).

[0177] 62. Zaid, B., Saidi, D., Benzaid, A. & Hadji, S. Effects of pH and chloride concentration on pitting corrosion of AA6061 aluminum alloy. *Corros. Sci.* 50, 1841-1847 (2008).

[0178] 63. Torbati-Sarraf, H., Torbati-Sarraf, S. A., Chawla, N. & Poursaee, A. A comparative study of corrosion behavior of an additively manufactured Al-6061 RAM2 with extruded Al-6061 T6. *Corros. Sci.* 174, 108838 (2020).

[0179] 64. de Wit, H. J., Wijenberg, C. & Crevecoeur, C. Impedance Measurements during Anodization of Aluminum. *J Electrochem. Soc.* 126, 779-785 (1979).

[0180] 65. Hsu, C. H. & Mansfeld, F. Concerning the Conversion of the Constant Phase Element Parameter Y0 into a Capacitance. *CORROSION* 57, 747-748 (2001).

[0181] 66. Rodriguez, M. A. & Carranza, R. M. Properties of the Passive Film on Alloy 22 in Chloride Solutions Obtained by Electrochemical Impedance. *J Electrochem. Soc.* 158, C221 (2011).

[0182] 67. Wang, L. et al. Insight into physical interpretation of high frequency time constant in electrochemical impedance spectra of Mg. *Corros. Sci.* 187, 109501 (2021).

[0183] 68. Zhou, X. et al. Copper enrichment in Al—Cu alloys due to electropolishing and anodic oxidation. *Thin Solid Films* 293, 327-332 (1997).

[0184] 69. Strehblow, H.-H., Melliar-Smith, C. M. & Augustyniak, W. M.

[0185] Examination of Aluminum-Copper Films during the Galvanostatic Formation of Anodic Oxide: II. Rutherford Backscattering and Depth Profiling. *J Electrochem. Soc.* 125, 915-919 (1978).

[0186] 70. Cornette, P., Zanna, S., Seyeux, A., Costa, D. & Marcus, P. The native oxide film on a model aluminium-copper alloy studied by XPS and ToF-SIMS. *Corros. Sci.* 174, 108837 (2020).

[0187] 71. Babu, A. P., Choudhary, S., Griffith, J. C., Huang, A. & Birbilis, N. On the corrosion of a high solute Al—Zn—Mg alloy produced by laser powder bed fusion. *Corros. Sci.* 189, 109626 (2021).

[0188] 72. Liu, M. et al. Electrochemical reactivity, surface composition and corrosion mechanisms of the complex metallic alloy Al_3Mg_2. *Corros. Sci.* 52, 562-578 (2010).

[0189] 73. Niverty, S., Kale, C., Solanki, K. N. & Chawla, N. Multiscale investigation of corrosion damage initiation and propagation in AA7075-T651 alloy using correlative microscopy. *Corros. Sci.* 185, 109429 (2021).

[0190] 74. Kairy, S. K. & Birbilis, N. Clarifying the Role of Mg_2Si and Si in Localized Corrosion of Aluminum Alloys by Quasi In Situ Transmission Electron Microscopy. *Corrosion* 76, 464-475 (2020).

[0191] 75. Zhao, Y. H., Liao, X. Z., Jin, Z., Valiev, R. Z. & Zhu, Y. T. Microstructures and mechanical properties of ultrafine grained 7075 Al alloy processed by ECAP and their evolutions during annealing. *Acta Mater.* 52, 4589-4599 (2004).

[0192] 76. Murayama, M. Microstructure of two-phase Al-1.7 at % Cu alloy deformed by equal-channel angular pressing. *Acta Mater.* 49, 21-29 (2001).

[0193] 77. Xu, C., Furukawa, M., Horita, Z. & Langdon, T. G. Influence of ECAP on precipitate distributions in a spray-cast aluminum alloy. *Acta Mater.* 53, 749-758 (2005).

[0194] 78. Wolverton, C. Solute-vacancy binding in aluminum. *Acta Mater.* 55, 5867-5872 (2007).

[0195] 79. Esquivel, J. & Gupta, R. K. Review-Corrosion-Resistant Metastable Al Alloys: An Overview of Corrosion Mechanisms. *J. Electrochem. Soc.* 167, 081504 (2020).

[0196] 80. Natishan, P. M. & O'Grady, W. E. Chloride Ion Interactions with Oxide-Covered Aluminum Leading to Pitting Corrosion: A Review. *J. Electrochem. Soc.* 161, C421-C432 (2014).

[0197] 81. Natishan, P. M. et al. Chloride Uptake by Oxide Covered Aluminum as Determined by X-Ray Photoelectron and X-Ray Absorption Spectroscopy. *J. Electrochem. Soc.* 146, 1737-1740 (1999).

[0198] 82. Galvele, J. R. Transport Processes and the Mechanism of Pitting of Metals. *J Electrochem. Soc.* 123, 464-474 (1976).

[0199] 83. Wang, S.-S. et al. Effect of Cu Content and Aging Conditions on Pitting Corrosion Damage of 7xxx Series Aluminum Alloys. *J Electrochem. Soc.* 162, C150-C160 (2015).

[0200] 84. Andreatta, F., Terryn, H. & de Wit, J. H. Corrosion behaviour of different tempers of AA7075 aluminium alloy. *Electrochimica Acta* 49, 2851-2862 (2004).

[0201] 85. McCafferty, E. A Surface Charge Model of Corrosion Pit Initiation and of Protection by Surface Alloying. *J Electrochem. Soc.* 146, 2863-2869 (1999).

[0202] 86. Gupta, R. K., Fabijanic, D., Zhang, R. & Birbilis, N. Corrosion behaviour and hardness of in situ consolidated nanostructured Al and Al—Cr alloys produced via high-energy ball milling. *Corros. Sci.* 98, 643-650 (2015).

[0203] 87. Birbilis, N. & Buchheit, R. G. Electrochemical Characteristics of Intermetallic Phases in Aluminum Alloys. *J. Electrochem. Soc.* 152, B140 (2005).

[0204] 88. Beura, V. K., Garg, P., Joshi, V. V. & Solanki, K. N. Numerical Investigation of Micro-Galvanic Corrosion in Mg Alloys: Role of the Cathodic Intermetallic Phase Size and Spatial Distributions. in *Magnesium Technology* 2020 (eds. Jordon, J. B., Miller, V., Joshi, V. V. & Neelameggham, N. R.) 217-223 (Springer International Publishing, 2020).

[0205] 89. Song, D. et al. Corrosion behaviour of bulk ultra-fine grained AZ91D magnesium alloy fabricated by equal-channel angular pressing. *Corros. Sci.* 53, 362-373 (2011).

[0206] 90. Osório, W. R., Moutinho, D. J., Peixoto, L. C., Ferreira, I. L. & Garcia, A. Macrosegregation and microstructure dendritic array affecting the electrochemical behaviour of ternary Al—Cu—Si alloys. *Electrochimica Acta* 56, 8412-8421 (2011).

[0207] 91. G01 Committee. Practice for Evaluating Intergranular Corrosion Resistance of Heat Treatable Aluminum Alloys by Immersion in Sodium Chloride+Hydrogen Peroxide Solution. http://www.astm.org/cgi-bin/resolver.cgi?G110-92R15.

Example 2

[0208] Modified Surface Attrition Treatment to Generate Corrosion-Resistant Gradient Nano-Grained Surface Layer Non-Limiting, Exemplary Disclosure Summary

[0209] Described herein is a method to create a gradient nano-grained surface layer on aluminum alloys without changing the overall composition of the alloy. Gradient nano-grained surface structures are surface structures of nanocrystalline grains whose magnitude in size increases the further from the surface you are which can improve corrosion resistance, strength and ductility in metals and metal alloys. Surface mechanical attrition treatment (SMAT) has been used to create gradient surface structures via impacts of a milling media at various temperatures. High-strength aluminum allow AA7075 was used in SMAT processing with Al-coated 440C stainless-steel balls at room temperature (RT) and liquid-nitrogen temperatures. Gradient microstructures were observed after milling, higher resistance, and improved corrosion resistance in the alloy was observed at

both processing temperatures though the alloy process at RT showed better overall properties.

[0210] AA7075 alloy was SMAT processed with 440C stainless-steel balls.

[0211] Gradient microstructures were formed in the alloy which resulted in higher surface resistance and higher corrosion resistance.

Example 3

[0212] Sol-SMAT-PA

[0213] An additional treatment named Sol-SMAT-PA was performed on circular disk samples besides RT SMAT and LN_2 SMAT. Non-limiting, exemplary details of the treatment are mentioned in the Table 5. Peak aging followed by SMAT treatment was performed to exploit the benefits of stored residual strains in the form of defects near the SMAT surface towards the diffusion of solute elements during aging.

TABLE 5

Non-limiting, exemplary processing methods

Treatment	Details
Sol-SMAT-PA	Solutionized at 475° C. for 2 hours followed by water quenching. SMAT with aluminum powder stainless steel balls for 30 mins at room temperature. Peak Aged at 120° C. for 24 hours followed by air cool.

[0214] Results and Discussion:

[0215] The cross-section and top surface of the Sol-SMAT-PA sample were characterized through SEM and the images are shown in FIG. **15**. The cross-section image shows the aluminum matrix without any major second-phase particles, unlike Base and RT SMAT samples. The top surface of the sample has only Al—Fe phases in the aluminum matrix. However, in the case of RT SMAT silicon, copper, and iron-rich micro-scale second phases were observed. It indicates that most of these solute elements can be present in the aluminum matrix without precipitating out as second phases. To further investigate the microstructural evolution TEM cross-sectional imaging along with their EDS compositional mapping was performed and the results are shown in FIG. **16**. TEM HAADF images show a gradient microstructure with smaller grains close to the SMAT surface. Few Fe and Si-rich sub-micron phases were observed along the grain boundaries of the aluminum matrix. However, in comparison to the RT SMAT sample, the volume fraction of sub-micron phases is significantly less in the Sol-SMAT-PA sample. This indicates that most of the solute elements i.e., Cu, Mg, Zn, Fe, Si are in the matrix without precipitating out as second-phase particles.

[0216] Electrochemical tests were performed to understand the effect of microstructural changes on the corrosion response of the Sol-SMAT-PA sample and the results were compared with base and RT SMAT samples. FIG. **17** panel a shows the potentiodynamic polarization curves for the samples. It can be observed that the Sol-SMAT-PA sample has the most positive corrosion potential and lowest corrosion current density. In comparison to RT SMAT a two orders magnitude drop in corrosion current density (corrosion rate) was observed in the Sol-SMAT-PA sample. Additionally, a quasi-passive region and a clear pitting potential in the Sol-SMAT-PA sample indicate its higher corrosion resistance. Similarly, FIG. **17** panel b illustrates the Nyquist plot for the Sol-SMAT-PA sample over different immersion times. The overall resistance of the surface layer can be represented by polarization resistance and the result is shown in FIG. **17** panel c. Sol-SMAT-PA samples have the highest Rp value after initial hours of oxide layer stabilization.

[0217] Overall, through this treatment, we have achieved a unique microstructure where most of the solute elements are present in the aluminum matrix and without wishing to be bound by theory, that with current or similar microstructure materials will have better corrosion resistance which can be attributed to stable oxide layer and reduced pitting corrosion. Without wishing to be bound by theory, similar microstructure can also be achieved through other processing techniques such as severe plastic deformation, solid-state processing, and heat treatments.

Example 4

[0218] Role of Gradient Nanograined Surface Layer on Corrosion Behavior of Aluminum 7075 Alloy

[0219] Surface Mechanical Attrition Treatment (FIG. **1**)

[0220] Al coating on stainless steel balls with pure aluminum powder

[0221] Surface mechanical attrition treatment (SMAT) in liquid nitrogen and room temperature environment

[0222] Gradient microstructure with significant change in, grain size, second phase composition and morphology

[0223] Surface and Cross section micrographs: SMAT (FIG. **2**)

[0224] Elongated grains were fragmented and plastically flowed

[0225] Presence of $Al_7Cu_2Fe/Al_{24}Fe_4Cu$ and Mg_2Si in base sample

[0226] Dissolution of inherent second phases and precipitation of new second phase

[0227] A non-uniform thickness of surface layer with different microstructure than underlying matrix

[0228] TEM micrograph of top surface: SMAT (FIG. **4**)

[0229] Grain fragmentation and grain boundary segregation of solute elements

[0230] precipitation of new Al—Cu, Cu—Si, and Zn phases

[0231] RT SMAT have smaller size of second phases

[0232] Vacancy binding tendency Si (0.08 eV)>Zn (0.03 eV)>Cu (0.02 eV)>Fe (~0.00)>Mg (−0.02)

[0233] Corrosion behavior of SMAT samples

[0234] Reduction in anodic and cathodic dissolution current density in SMAT alloys (FIG. **6**)

[0235] Stable oxide layer

[0236] Higher pitting resistance

[0237] EIS fitting equivalent circuit (FIG. **19**)

[0238] Time dependent Nyquist plots for three alloys (FIG. **7**)

[0239] With increase in time gradual drop in overall diameter of Nyquist curve can be observed

[0240] RT SMAT showed higher film resistance throughout the duration of immersion

[0241] ToF-SIMS analysis top surface film SMAT (FIG. **10**)

[0242] Samples were immersed in 0.6 M NaCl for 15 minutes and then dried

[0243] Formulation of aluminum hydroxide:

$$Al \rightarrow Al^{3+} + +3e^{-}$$

$$O^{2} + H_2O + 4e^{-} \rightarrow 4OH^{-}$$

$$Al^{3+} + 3OH^{-} \rightarrow Al(OH)_3$$

[0244] Enrichment of Cu in SMAT oxide layer

[0245] Increase in SiO_2 in SMAT oxide layer

[0246] SiO_2 will lower the overall iso electric point (ISP) of the oxide layer and adsorption tendency of Cl^- (FIG. **20**)

[0247] pH of electrolyte lower than oxide layer ISP

$$-MOH_{surf} + H_{aq}^{+} \leftrightarrow -MOH_{2\ surf}^{+}$$

[0248] pH of electrolyte higher than oxide layer ISP

$$-MOH_{surf} + OH_{aq}^{-} \leftrightarrow -MO_{surf}^{-} + H_2O$$

[0249] Corrosion Surface Characterization (FIG. **11**)

[0250] Base sample shows pitting (red arrow) and intergranular dissolution (green arrow)

[0251] Deposition of corrosion products (yellow arrow) in all samples

[0252] Severity of corrosion damage is higher in base sample

[0253] Non-Limiting Results

[0254] SMAT resulted in a gradient microstructure with significant change in, grain size, second phase composition and morphology

[0255] Dissolution of inherent phases and precipitation of new phases were observed

[0256] RT SMAT surface showed higher film resistance than others and can be attributed to thick composite oxide layer, type and distribution of second phase particles EQUIVALENTS

[0257] Those skilled in the art will recognize, or be able to ascertain, using no more than routine experimentation, numerous equivalents to the specific substances and procedures described herein. Such equivalents are considered to be within the scope of this invention and are covered by the following claims.

What is claimed is:

1. A method of producing a gradient nano-grained surface layer on an alloy comprising:

obtaining a milling media and a base alloy;

coating the milling media in a powder; and

subjecting the base alloy to surface mechanical attrition treatment (SMAT) by impacting the alloy with the coated milling media to generate a SMAT alloy with a gradient nano-grained surface layer.

2. The method of claim **1**, wherein the base alloy is subjected to heat treatment or is not subjected to heat treatment.

3. The method of claim **2**, wherein the heat treatment comprises solutionization, aging treatment, or a combination thereof.

4. The method of claim **2**, wherein the alloy is subjected to heat treatment before SMAT, subjected to heat treatment after SMAT, or subjected to heat treatment both before and after SMAT.

5. The method of claim **1**, wherein the milling media comprises stainless steel.

6. The method of claim **5**, wherein the stainless steel comprises 440C stainless steel.

7. The method of claim **1**, wherein the base alloy comprises an aluminum alloy.

8. The method of claim **7**, wherein the base alloy comprises 7075 aluminum alloy, 2024 aluminium alloy, 5083 aluminium alloy, and 6061 aluminium alloy.

9. The method of claim **1**, wherein the powder comprises elements which do not induce more cathodic precipitates.

10. The method of claim **7**, wherein the powder comprises a metal found in the base alloy.

11. The method of claim **8**, wherein the metal comprises aluminum.

12. The method of claim **1**, wherein the powder comprises a metal not found in the base alloy, a metal found in the base alloy, an element, a combination of elements, a ceramic powder, carbide, or combination thereof.

13. The method of claim **12**, wherein the metal comprises aluminum, magnesium, magnesium, copper, iron, chromium, titanium, zinc, scandium, vanadium, cobalt, nickel, silicon, or a combination thereof.

14. The method of claim **1**, wherein the surface mechanical attrition treatment (SMAT) is performed at room temperature or liquid-nitrogen (LN_2) cooled temperature.

15. The method of any one of claims **1-14**, wherein the SMAT alloy has improved corrosion resistance compared to the base alloy.

16. The method of any one of claims **1-14**, wherein the SMAT alloy has improved surface resistance compared to the base alloy.

17. The method of any one of claims **1-11** or **14-16**, wherein the elemental components of the SMAT alloy are not changed compared to the base alloy.

18. A SMAT alloy produced by the method of any one of claims **1-17**.

19. The SMAT alloy of claim **18**, wherein the SMAT alloy has improved corrosion resistance compared to an untreated alloy.

20. The SMAT alloy of claim **18**, wherein the SMAT alloy has improved surface resistance compared to an untreated alloy.

21. The SMAT alloy of claim **18**, wherein the SMAT alloy has a higher thickness of oxide layer compared to an untreated alloy when exposed to a corrosive agent.

* * * * *